Supporting Information

Unveiling selectivity trends for CO_2 reduction reaction over $Ti_3C_2T_x$ MXene: The key role of less-stable intermediate states and coadsorbates

Pablo Lozano-Reis[1], **Kai S. Exner**[1,2,3,*]

[1] *University of Duisburg-Essen, Faculty of Chemistry, Theoretical Catalysis and Electrochemistry, Universitätsstraße 5, 45141 Essen, Germany*

[2] *Cluster of Excellence RESOLV, 44801 Bochum, Germany*

[3] *Center for Nanointegration (CENIDE) Duisburg-Essen, 47057 Duisburg, Germany*

* Corresponding author: kai.exner@uni-due.de ORCID: 0000-0003-2934-6075

S1. Computational details

To determine the energetics of the CO_2 reduction reaction (CO_2RR) and the hydrogen evolution reaction (HER) on different $Ti_3C_2T_x$ (T_x = *OH and/or *F) model systems, periodic DFT calculations have been carried out using the Vienna Ab-initio Simulation Package (VASP) code **[1-3]**. All calculations have been performed using the Perdew – Burke – Ernzerhof (PBE) exchange correlation functional **[4]** alongside Grimme's D3 term to account for dispersion effects **[5]**. The frozen-core augmented (PAW) **[6]** method is used to describe the interaction between the atomic cores and the valence electron density. The Brillouin zone has been sampled with a (5×5×1) ***k***-point mesh generated via the **Γ**-centered method and a cutoff energy of 440 eV has been used for the plane wave basis expansion. The electronic energy and ionic relaxation criterion have been selected to 10^{-5} eV and 0.01 eV $Å^{-1}$, respectively. Transition state (TS) have been located using the Catlearn Bayesian transition state search module (ML-NEB) **[7]**. Note that due to convergence problems, the force criterion used for the calculation of some TSs has been set to 0.05 eV $Å^{-1}$. These TSs are properly identified throughout the text or tables. Frequency calculations have been performed to ensure that all adsorbates and coadsorbate states correspond to real minima one the potential energy surface, while the located TS correspond to a saddle point on the potential energy surface, its imaginary frequency corresponding to the reaction coordinate.

The $Ti_3C_2T_x$ (T_x = *OH and/or *F) MXene surface models consists of an appopriate (3×3) $Ti_3C_2(0001)$ supercell with different terminal (T_x) groups adsorbed on top of the MXene surface. A vacuum of at least 20 Å in the perpendicular direction to the surface has been placed to avoid spurious interactions between periodically repeated replicas. The slab models were asymmetric, and thus the dipole correction was applied **[8]**. From the DFT calculations, we have derived the Gibbs free-energy of the different states as detailed in subsection S1.1. We tested the effect of spin polarization and found non-significant changes in the activity descriptor $G_{\max}(U)$ as described in detail in the following subsection S1.2. These results are in line with previous findings showing a minimal effect of spin polarization in functionalized MXene surface **[9]**. Therefore, we rely on non-spin polarized calculations to study the CO_2RR and HER on $Ti_3C_2T_x$ MXene surfaces. Moreover, we have also tested the effect of the electrolyte, which is included using the VASPSol **[10,11]** extension of the VASP software. As detailed in subsection S1.2, minimal differences in the free energy were observed, and therefore solvation was not considered in the presented analysis.

S1.1 Calculation of Gibbs free energy

The Gibbs free energy of state *i* (G_i) at $U = 0$ V vs RHE, is calculated using the following relation:

$$G_i = E_i^{DFT} + E_i^{ZPE} - TS_i \tag{S1}$$

where E_i^{DFT}, E_i^{ZPE} and S_i denote the electronic energy derived from DFT calculations, the zero-point energy (ZPE) and the entropy of state *i*, respectively. *T* refers to the temperature, which is choosen to be 298.15 K in our analysis. Note that for the gas-phase molecules, the entropy term is obtained from thermodynamic tables **[12]** and includes translational, rotational and vibrational contributions to the entropy. For adsorbed intermediates, it is a common approach to consider that the 3N degrees of freedom (N refers to the number of atoms of the intermediate), correspond to vibrations, since translational and rotational modes are now frustrated. Therefore, the 3N vibrational modes are used to determine the ZPE and the vibrationl entropy of adsorbed intermediates. Note that low frequencies modes can lead to exceedingly large vibrational contributions to entropy as explained in ref **13**. Therefore, low frequency modes have been set to a cutoff value of 6.9 meV **[13]**. Finally, one must advert that the ZPE and vibrational entropy of the substrate is not considered both for the empty substrate as well as the adsorbate on top of the substrate. This is a common approach and means that material phonons are decoupled with adsorabte contributions. The formulas used to compute the ZPE and vibrationl entropy (S_i^{vib}) are **[9]**:

$$E_i^{ZPE} = \frac{1}{2}\sum_k^{3N} \nu_i^k \tag{S2}$$

$$S_i^{vib} = k_B \sum_k^{3N} \frac{\frac{\nu_i^k}{k_B T}}{e^{\frac{\nu_i^k}{k_B T}}-1} - \ln\left(1 - e^{-\frac{\nu_i^k}{k_B T}}\right) \qquad \text{(S3)}$$

where k_B is the Boltzmann constant in eV K^{-1}, ν_i^k is the frequency associated to the k frequency mode of i adsorbate in eV, and T is the temperature in K. Importantly, one should consider that the Gibbs free energy of a species i is potential dependent, and its free energy changes as a function of the number of proton-electron transfer steps (ν_e) and the applied electrode potential as follows:

$$G_i(U) = G_i(0) + \nu_e \times e \times U \qquad \text{(S4)}$$

where $G_i(0)$ is the Gibbs free energy of species i at $U = 0$ V vs. RHE (i.e., the one calculated using equation S1).

S1.2 Impact of spin polarization and solvation

We have verified our approach and conclusions by quantifying the impact of spin polarization and solvation, the latter included via the VASPsol extension **[10,11]**. To do so, we have carried out two sets of calculation for the CO_2RR and HER for two different surfaces (i.e., Ti_3C_2-7*OH and Ti_3C_2-1*OH-6*F). The first set of calculations include the spin-polarization while the second includes the solvation effect. **Table S1** and **S2** summarize the results at $U = -0.4$ V vs. RHE for the Ti_3C_2-7*OH and Ti_3C_2-1*OH-6*F surfaces, respectively.

Table S1. Activity descriptor G_{max} and limiting span for the different CO_2RR and HER products for the Ti_3C_2-7*OH surface at $U = -0.4$ V vs RHE. Calculations without including spin polarization (spin restricted), including spin polarization (spin unrestricted), and including solvation (VASPsol) are considered.

$U = -0.4$ V vs RHE	**DFT (spin restricted)**		**DFT (spin unrestricted)**		**DFT + Vaspsol**	
	G_{max} / eV	**Limiting Span**	**G_{max} / eV**	**Limiting Span**	**G_{max} / eV**	**Limiting Span**
$H_{2(g)}$	0.61	$*H \rightarrow H_{2(g)}$	0.57	$*H \rightarrow H_{2(g)}$	0.64	$*H \rightarrow H_{2(g)}$
$CO_{(g)}$	1.62	$*CO_2 \rightarrow CO_{(g)}$	1.63	$*CO_2 \rightarrow CO_{(g)}$	1.37	$*CO_2 \rightarrow CO_{(g)}$
$HCOOH_{(l)}$	1.71	$*HCOOH \rightarrow HCOOH_{(aq)}$	1.68	$*HCOOH \rightarrow HCOOH_{(aq)}$	1.77	$*HCOOH \rightarrow HCOOH_{(aq)}$
$CH_3OH_{(aq)}$	0.70	$*CO_2 \rightarrow HOOC$	0.71	$*CO_2 \rightarrow HOOC$	0.45	$*HCOO \rightarrow *HCOH$
$CH_{4(g)}$	0.68	$*O \rightarrow CH4(g)$	0.70	$*O \rightarrow CH4(g)$	0.45	$*HCOO \rightarrow *HCOH$

Table S2. Activity descriptor G_{max} and limiting span for the different CO_2RR and HER products for the Ti_3C_2-1*OH-6*F surface at U = -0.4 V vs RHE. Calculations without including spin polarization (spin restricted), including spin polarization (spin unrestricted), and including solvation (VASPsol) are considered.

***U* = -0.4 V vs RHE**	**DFT (spin restricted)**		**DFT (spin unrestricted)**		**DFT + Vaspsol**	
	G_{max} / eV	**Limiting Span**	**G_{max} / eV**	**Limiting Span**	**G_{max} / eV**	**Limiting Span**
$H_{2(g)}$	0.62	$*H \rightarrow H_{2(g)}$	0.64	$*H \rightarrow H_{2(g)}$	0.20	$*H \rightarrow H_{2(g)}$
$CO_{(g)}$	0.92	$*CO \rightarrow CO_{(g)}$	0.94	$*CO \rightarrow CO_{(g)}$	0.33	$*CO \rightarrow CO_{(g)}$
$HCOOH_{(aq)}$	1.63	$*HCOOH \rightarrow HCOOH_{(aq)}$	1.64	$*CO_2 \rightarrow HCOOH_{(aq)}$	0.86	$*HCOOH \rightarrow HCOOH_{(aq)}$
$CH_3OH_{(aq)}$	0.39	$*CH_2OH \rightarrow CH_3OH_{(aq)}$	0.40	$*CH_2OH \rightarrow CH_3OH_{(aq)}$	0.05	$*CO_2 \rightarrow *HOOC$
$CH_{4(g)}$	0.14	$*CH_3 \rightarrow *CH_{4(g)}$	0.15	*CH3 → *CH4(g)	0.05	$*CO_2 \rightarrow *HOOC$

From the results in **Table S1** and **S2**, it is evident that the consideration of spin polarization does not result in significant differences in the activity descriptor $G_{max}(U)$, in line with previous studies in similar systems **[9]**. Regarding the solvation effect, a similar observation is made. While the absolute G_{max} values change, the selectivity predictions remain unchanged, with the only exception of H_2 selectivity for the Ti_3C_2-7*OH surface, where selectivity is underestimated. We attribute this difference to a lower CO_2 adsorption energy when including solvation so that in turn CO_2RR is favored. As no significant deviations are observed when accounting for spin polarization or solvation in our computational protocol, we believe that our approach is sufficient to qualitatively understand the differences in the CO_2RR over $Ti_3C_2T_x$ surfaces.

S2. Elementary steps for CO_2RR and HER

For the investigation of the CO_2RR to different C_1 products, we have included the elementary steps listed in equations (S5) – (S34). Note that for some intermediate states, we have considered different possible configurations in our calculations, which differ on its orientation while the type of elementary step is essentially the same. Therefore, we have not counted such possibilities twice in the following elementary steps. Note that the elementary steps marked in blue refer to steps in which a product is formed.

$$* + CO_{2(g)} \rightarrow *CO_2 \qquad \text{(S5)}$$

$$*CO_2 + H^+ + e^- \rightarrow *COOH \qquad \text{(S6)}$$

$$*COOH + H^+ + e^- \rightarrow *CO + H_2O_{(l)} \qquad \text{(S7)}$$

$$*CO \rightarrow CO_{(g)} + * \qquad \text{(S8)}$$

$$*CO_2 + H^+ + e^- \rightarrow *HCOO \qquad \text{(S9)}$$

$$*COOH + H^+ + e^- \rightarrow *HCOOH \qquad \text{(S10)}$$

$$*HCOO + H^+ + e^- \rightarrow *HCOOH \qquad \text{(S11)}$$

$$*HCOOH \rightarrow HCOOH_{(aq)} \qquad \text{(S12)}$$

$$*HCOOH + H^+ + e^- \rightarrow *HCO + H_2O_{(l)} \qquad \text{(S13)}$$

$$*CO + H^+ + e^- \rightarrow *HCO \qquad \text{(S14)}$$

$$*CO + H^+ + e^- \rightarrow *COH \qquad \text{(S15)}$$

$$*HCO + H^+ + e^- \rightarrow *HCOH \qquad \text{(S16)}$$

$$*HCO + H^+ + e^- \rightarrow *CH_2O \qquad \text{(S17)}$$

$$*COH + H^+ + e^- \rightarrow *HCOH \qquad \text{(S18)}$$

$$*COH + H^+ + e^- \rightarrow *C + H_2O_{(l)} \qquad \text{(S19)}$$

$$*CH_2O + H^+ + e^- \rightarrow *CH_2OH \qquad \text{(S20)}$$

$$*CH_2O + H^+ + e^- \rightarrow *CH_3O \qquad \text{(S21)}$$

$$*HCOH + H^+ + e^- \rightarrow *CH_2OH \qquad \text{(S22)}$$

$$*HCOH + H^+ + e^- \rightarrow *CH + H_2O_{(l)} \qquad \text{(S23)}$$

$$*C + H^+ + e^- \rightarrow *CH \qquad \text{(S24)}$$

$$*CH_3O + H^+ + e^- \rightarrow CH_3OH_{(l)} \qquad \text{(S25)}$$

$$*CH_3O + H^+ + e^- \rightarrow *O + CH_{4(g)} \quad (S26)$$

$$*CH_2OH + H^+ + e^- \rightarrow CH_3OH_{(aq)} \quad (S27)$$

$$*CH + H^+ + e^- \rightarrow *CH_2 \quad (S28)$$

$$*O + H^+ + e^- \rightarrow *OH \quad (S29)$$

$$*CH_2 + H^+ + e^- \rightarrow *CH_3 \quad (S30)$$

$$*OH + H^+ + e^- \rightarrow * + H_2O_{(l)} \quad (S31)$$

$$*CH_3 + H^+ + e^- \rightarrow * + CH_{4(g)} \quad (S32)$$

Finally, we have also included the HER as a competing reaction channel in our analysis. The elementary steps considered for HER are given in equations (S32) – (S33).

$$* + H^+ + e^- \rightarrow *H \quad (S33)$$

$$*H + H^+ + e^- \rightarrow H_{2(g)} \quad (S34)$$

S3. Formation Gibbs free energies

The use of formation energies (or formation Gibbs free energies if the Gibbs free energy for the reference and calculated species is used) instead of adsorption energies is useful because they provide an easy and normalized way to construct free-energy diagrams while still providing useful information about the interaction of an intermediate with the surface. Formation energies represent energy differences with respect to a reference set that should be chosen following the next rules:

- The catalysts (i.e., the surface in which the reactivity occurs) is included in the reference set.
- The rest of the reference species are gas-phase species. The number of gas-phase species needed in the reference set depends on the number of different atoms encountered in the intermediate states of the reaction mechanisms.
- The reference gas-phase species must have linearly independent compositions, which implies that we should not be able to write a reaction that produces a reference species from another reference species.

In our study, we have C-, H- and O- containing species as well as 7 different surfaces; thus, a good reference set is {surface, $H_{2(g)}$, $CO_{2(g)}$, $H_2O_{(g)}$}, where surface will change depending on the considered surface model (see **Figure 1** in the main text). From the gas-phase molecules, the reference energy per atom (R_j) is calculated as follows:

$$R_H = \frac{1}{2}\, G_{H_{2(g)}} \tag{S35}$$

$$R_O = G_{H_2O_{(g)}} - 2R_H \tag{S36}$$

$$R_C = G_{CO_{2(g)}} - 2R_O \tag{S37}$$

where $G_{i(g)}$ is the Gibbs free energy for the gas-phase species (see Section S1.1 for a detailed description on how Gibbs free energies are calculated). Then, the formation Gibbs free energy of an adsorbate *i* (G_i^f) is defined as:

$$G_i^f = G_{i-slab} - E_{surface} - \sum_j \left(n_j R_j\right) \tag{S38}$$

where G_{i-slab} is the Gibbs free energy of adsorbate *i* on the surface, E_{surface} is the energy of the surface (because for surfaces, the ZPE and entropy are neglected), n_j is the number of atoms *j* in species *i* and R_j is the reference energy of atom *j*. For instance, the formation Gibbs free energy of *COH adsorbed on the Ti_3C_2-4*OH*3F at *U* = 0 V vs RHE is:

$$G^f\left({}^*COH_{Ti_3C_2-{}^*4OH-{}^*3F} \right) =$$

$$G\left({}^*COH_{Ti_3C_2-{}^*4OH-{}^*3F} \right) - E_{Ti_3C_2-{}^*4OH-{}^*3F} - R_C - R_O - R_H \qquad \text{(S39)}$$

Interestingly, as $H_{2(g)}$ is used as a reference molecule and we adopt the computational hydrogen electrode **[14]** approach to describe proton-coupled electron transfer steps, the free energy change of a proton-electron transfer step is just the difference between the formation Gibbs free energy of the final and initial states. Note that the effect of the applied potential can be included by considering the Gibbs free energy (G_i) of the intermediate at the specific potential using equation S4 (see section S1).

S4. Gas-phase error corrections

To correctly represent the thermodynamics of the CO_2RR, gas-phase error corrections **[15,16]** have been applied. The total DFT gas-phase errors (ε_T) can be derived by comparing the experimental and DFT-based calculated Gibbs free energy of a reaction in the gas phase:

$$\varepsilon_T = \Delta_r G_{DFT} - \Delta_r G_{exp} \tag{S40}$$

The total DFT error results from the errors of the products (ε_P) and reactants (ε_R):

$$\varepsilon_T = \sum \varepsilon_P - \sum \varepsilon_R \tag{S41}$$

In order to calculate the gas-phase error of a particular molecule, the formation reaction of the given molecule from its elements in their standard states is considered and compared with the experimental value. In our particular case, the gas-phase molecules are composed of H, O, and C atoms. Therefore, the formation reaction of a generic gaseous compound ($H_\alpha C_\beta O_\gamma$) from its elements can be written as:

$$\frac{\alpha}{2} H_2 + \beta C + \frac{\gamma}{2} O_2 \longrightarrow H_\alpha C_\beta O_\gamma \tag{S42}$$

It is commonly assumed that DFT yields good predictions for hydrogen and graphene so that the error for C and H_2 is equal to 0 (ε_C= 0 and ε_{H_2}= 0). The error of O_2 is calculated from the water formation reaction ($2H_2 + O_2 \rightarrow 2H_2O$) assuming that the error in the calculated DFT energy of water is negligible. Combining equations (S42) and (S43), we refer the error of the O_2 molecule to the following relation:

$$\varepsilon_{O_2} = -(\Delta_r G_{DFT}^{WFR} - \Delta_r G_{exp}^{WFR}) = \text{-0.46 eV} \tag{S43}$$

Afterwards, the DFT energy of the C, H_2, and O_2 compounds is corrected for their errors (i.e., 0 eV, 0 eV and -0.46 eV, respectively). Subsequently, the gas-phase error of a generic $H_\alpha C_\beta O_\gamma$ molecule is calculated from its experimental Gibbs free energy of formation and the one obtained from the DFT calculations after correcting the C, H_2, and O_2 energies. Finally, the DFT energy of the generic $H_\alpha C_\beta O_\gamma$ molecule is corrected by subtracting the gas-phase error. **Table S3** summarizes the gas-phase errors for the relevant molecules used in this work.

Table S3. Gas-phase errors for reactant and product molecules of CO_2RR and HER calculated from its experimental and DFT-based calculated Gibbs free energy of formation.

Molecule	ε_T / eV
CO_2	-0.16
CO	0.26
CH_4	0.03
HCOOH	-0.17
CH_3OH	-0.03
H_2	0.0
H_2O	0.0

S5. CO_2RR to HCOOH under different pH conditions

HCOOH is a weak acid and depending on the pH conditions, it can be found in its protonated or deprotonated form (i.e., HCOOH or $HCOO^-$), respectively. The pK_a of HCOOH is 3.75, which means that at pH values above 3.75, the predominant species is $HCOO^-$ rather than HCOOH. To evaluate the effect of the pH on the HCOOH formation **[17]**, we calculate the G_{max} at U = -0.4 vs RHE at three different pH conditions (i.e., pH = 0, 7 and 14) for two different MXene surfaces (i.e., Ti_3C_2-7*OH and Ti_3C_2-1*OH-6*F) as shown in **Figure S1**.

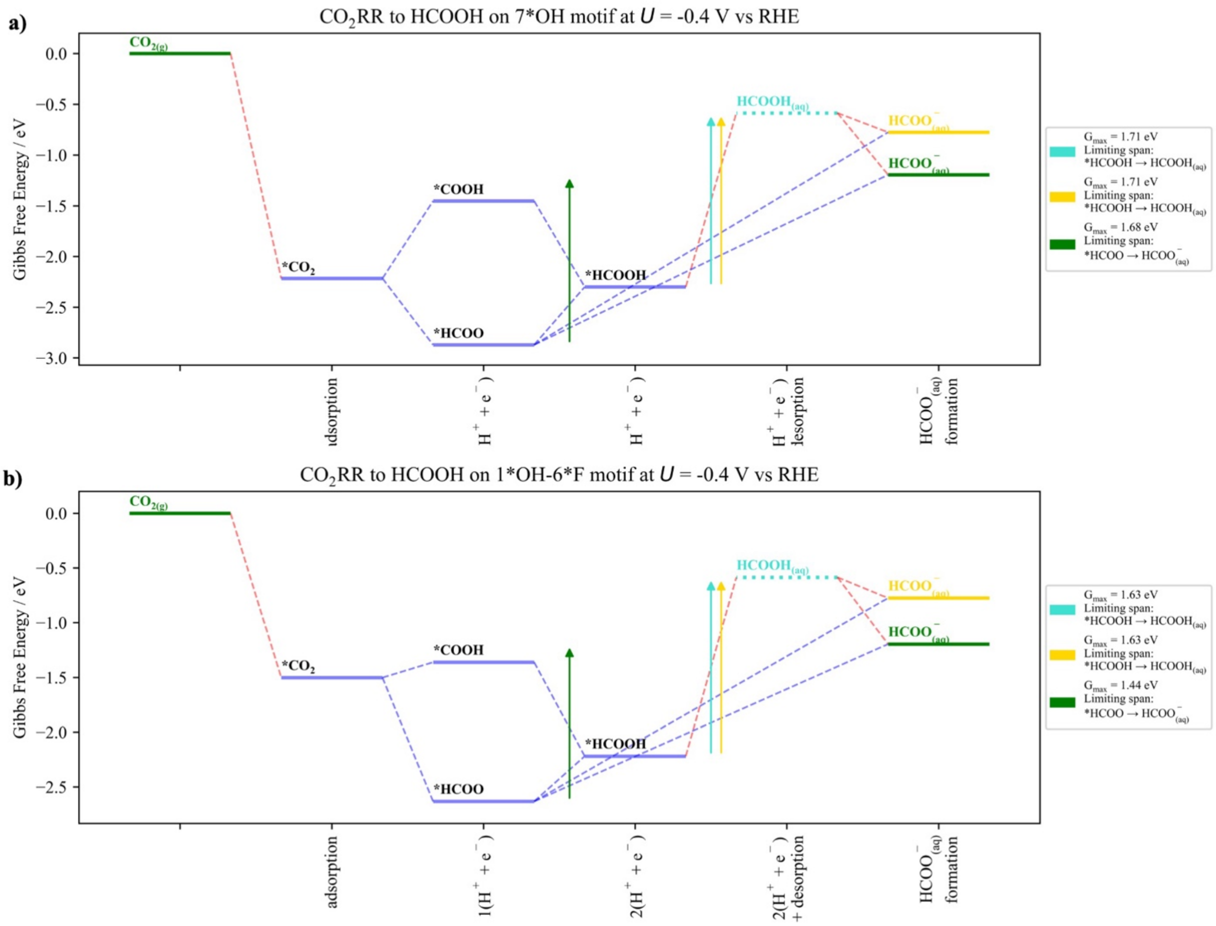

Figure S1. Gibbs free energy diagram for CO_2RR to HCOOH at U = -0.4 V vs RHE of **a)** Ti_3C_2-7*OH surface model and **b)** Ti_3C_2-1*OH-6*F surface model. Cyan, gold and green arrows are used to schematically represent the limiting span for the CO_2RR to $HCOOH_{(aq)}$ at pH = 0, 7 and 14, respectively. Details on the G_{max} and intermediates involved in the limiting span for each reaction are shown in the right legend.

From **Figure S1** it is evident that neutral conditions do not affect the $G_{max}(U)$ value, whereas alkaline conditions slightly reduce $G_{max}(U)$. As the experiments **[18]** are performed at pH ≈ 7 – 8, we conclude that no differences in selectivity are expected. Therefore, for simplicity, we consider HCOOH in our analysis.

S6. Activity descriptor $G_{max}(U)$

In computational catalysis, it is common to derive catalytic activity and selectivity based on the analysis of the free energy-diagrams. In particular, in computational electrocatalysis, a common assumption is to rely on Brønsted -Evans-Polanyi (BEP) relations **[19-21]**, which correlate thermodynamics with kinetics. Therefore, free-energy diagrams are constructed based on the thermodynamics of the different intermediates, which allow predicting the activity and selectivity of a given catalyst.

The most widely used descriptor for the electrocatalytic activity in this context is the thermodynamic overpotential **[14]**, which refers to the elementary reaction step with the highest free-energy change at the equilibrium potential of the given reaction. The thermodynamic overpotential (η_{TD}) provides a basis for determining the limiting potential (U_{lim}) **[22]**, which represents the applied potential at which all the elementary proton-coupled electron transfer steps become either thermoneutral or exergonic. The activity predictions based on the thermodynamic overpotential rely on the tacit assumption that a single elementary step, which is determined at the reaction equilibrium potential, limits the reaction rate. However, the above assumptions are not always fulfilled, as product formation require the application of a finite overpotential **[23,24]**, or multiple steps can contribute to the overall reaction rate **[25]**.

To address these limitations, Exner, inspired by the earlier work of Kozuch and Shaik in the context of homogeneous catalysis **[26]**, proposed an alternative descriptor, $G_{max}(U)$ **[27,28]**. This descriptor includes overpotential and kinetic effects into the activity analysis. $G_{max}(U)$ enables a potential-dependent analysis of activity trends by examining all possible free-energy spans between consecutive intermediates for a given mechanism at a given potential (U). This methodology is outlined for the followimg mechanism of CO_2RR to CH_3OH.

$$* + CO_{2(g)} \rightarrow *CO_2 \tag{S44}$$

$$*CO_2 + H^+ + e^- \rightarrow *HOOC \tag{S45}$$

$$*HOOC + H^+ + e^- \rightarrow *CO + H_2O_{(l)} \tag{S46}$$

$$*CO + H^+ + e^- \rightarrow *HCO \tag{S47}$$

$$*HCO + H^+ + e^- \rightarrow *HCOH \tag{S48}$$

$$*HCOH + H^+ + e^- \rightarrow *CH_2OH \tag{S49}$$

$$*CH_2OH + H^+ + e^- \rightarrow CH_3OH_{(aq)} \tag{S50}$$

Based on the above mechanism, the $G_{\max}(U)$ is calculated from the potential-dependent Gibbs free energies of the different reaction intermediates, namely: $*CO_2$, *HOOC, *CO, *HCO, *HCOH, $*CH_2OH$ and $CH_3OH_{(aq)}$, which are derived from DFT as explained in Section S1.1. Then, based on the potential-dependent free energies and the specific mechanism of a given reaction channel, the different free-energy spans are defined by equations (S51) – (S71):

$$G_{span\#1}(U) = G_{*HOOC}(U) - G_{*CO_2}(U) \tag{S51}$$

$$G_{span\#2}(U) = G_{*CO}(U) - G_{*CO_2}(U) \tag{S52}$$

$$G_{span\#3}(U) = G_{*COH}(U) - G_{*CO_2}(U) \tag{S53}$$

$$G_{span\#4}(U) = G_{*HCOH}(U) - G_{*CO_2}(U) \tag{S54}$$

$$G_{span\#5}(U) = G_{*CH_2OH}(U) - G_{*CO_2}(U) \tag{S55}$$

$$G_{span\#6}(U) = G_{*CH_3OH_{(aq)}}(U) - G_{*CO_2}(U) \tag{S56}$$

$$G_{span\#7}(U) = G_{*CO}(U) - G_{*HOOC}(U) \tag{S57}$$

$$G_{span\#8}(U) = G_{*COH}(U) - G_{*HOOC}(U) \tag{S58}$$

$$G_{span\#9}(U) = G_{*HCOH}(U) - G_{*HOOC}(U) \tag{S59}$$

$$G_{span\#10}(U) = G_{*CH_2OH}(U) - G_{*HOOC}(U) \tag{S60}$$

$$G_{span\#11}(U) = G_{*CH_3OH_{(aq)}}(U) - G_{*HOOC}(U) \tag{S61}$$

$$G_{span\#12}(U) = G_{*COH}(U) - G_{*CO}(U) \tag{S62}$$

$$G_{span\#13}(U) = G_{*HCOH}(U) - G_{*CO}(U) \tag{S63}$$

$$G_{span\#14}(U) = G_{*CH_2OH}(U) - G_{*CO}(U) \tag{S64}$$

$$G_{span\#15}(U) = G_{*CH_3OH_{(aq)}}(U) - G_{*CO}(U) \tag{S65}$$

$$G_{span\#16}(U) = G_{*HCOH}(U) - G_{*COH}(U) \tag{S66}$$

$$G_{span\#17}(U) = G_{*CH_2OH}(U) - G_{*COH}(U) \tag{S67}$$

$$G_{span\#18}(U) = G_{*CH_3OH_{(aq)}}(U) - G_{*COH}(U) \tag{S68}$$

$$G_{span\#19}(U) = G_{*CH_2OH}(U) - G_{*HCOH}(U) \tag{S69}$$

$$G_{span\#20}(U) = G_{*CH_3OH_{(aq)}}(U) - G_{*HCOH}(U) \tag{S70}$$

$$G_{span\#21}(U) = G_{*CH_3OH_{(aq)}}(U) - G_{*CH_2OH}(U) \tag{S71}$$

The descriptor $G_{\max}(U)$ is defined as the largest free-energy span extracted from the set of all spans considered.

$$G_{max}(U) = max\{G_{span\#k}(U), k = 1, \dots, n\} \tag{S72}$$

A graphical representation in terms of a free-energy diagram with the $G_{\max}(U)$ value and limiting span for three applied potentials (i.e., $U = 0$, -0.2 and -0.4 V vs RHE) is shown using the example of the CO_2RR to CH_3OH on the Ti_3C_2-3*OH-4*F surface in **Figure S2**, **S3**, and **S4**.

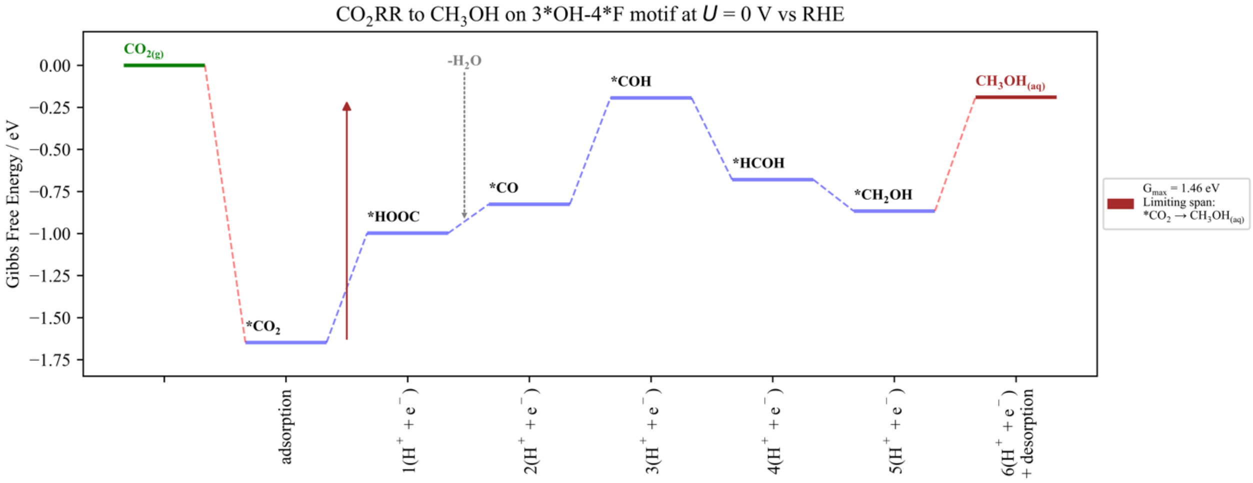

Figure S2. Gibbs free energy diagram for CO_2RR to CH_3OH of the Ti_3C_2-3*OH-4*F surface model at $U = 0$ V vs RHE. Brown arrow is used to schematically represent the limiting span. Details on the $G_{\max}$ and intermediates involved in the limiting span for each reaction are shown in the legend.

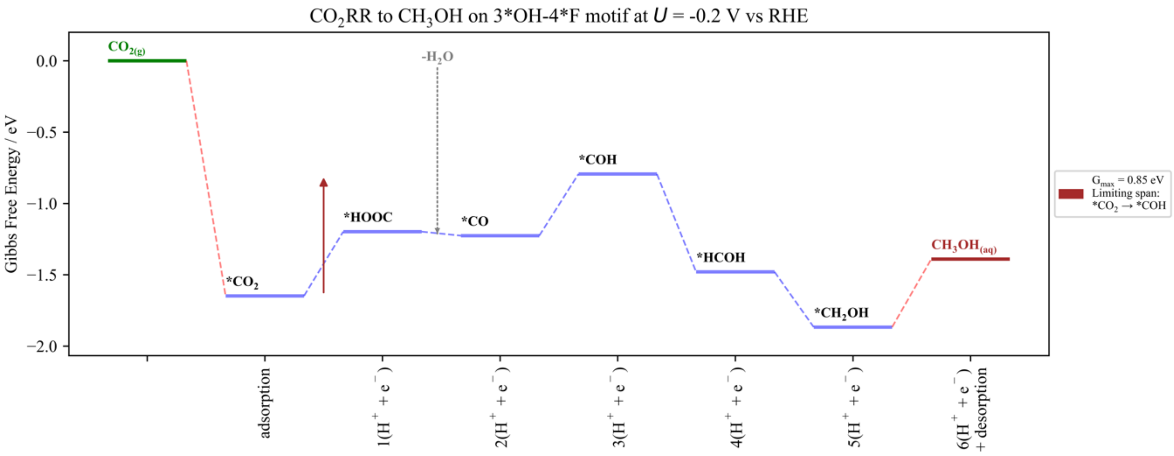

Figure S3. Gibbs free energy diagram for CO$_2$RR to CH$_3$OH of the Ti$_3$C$_2$-3*OH-4*F surface model at U = -0.2 V vs RHE. Brown arrow is used to schematically represent the limiting span. Details on the G_{max} and intermediates involved in the limiting span for each reaction are shown in the legend.

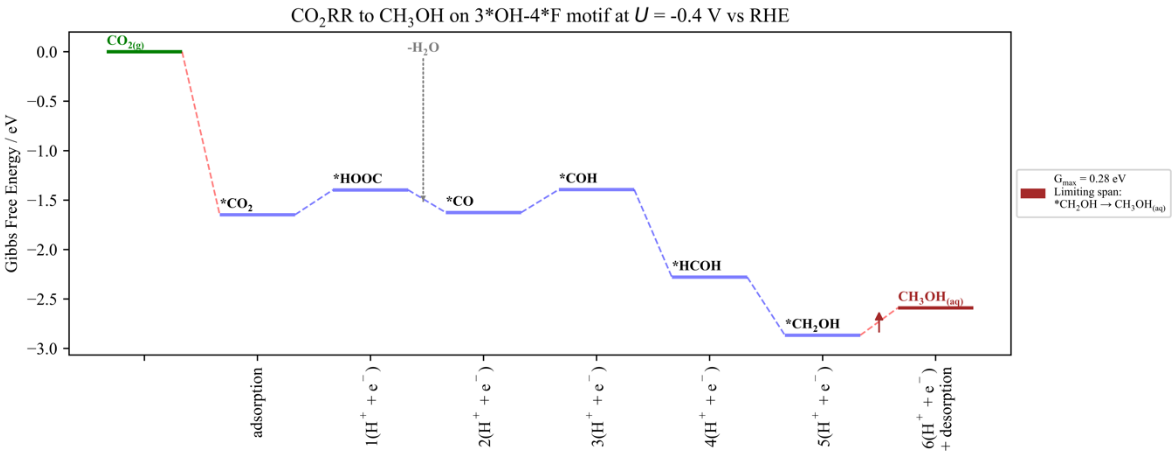

Figure S4. Gibbs free energy diagram for CO$_2$RR to CH$_3$OH of the Ti$_3$C$_2$-3*OH-4*F surface model at U = -0.4 V vs RHE. Brown arrow is used to schematically represent the limiting span. Details on the G_{max} and intermediates involved in the limiting span for each reaction are shown in the legend.

S7. CO_2RR and HER free energy diagrams and potential dependency for the different $Ti_3C_2T_x$ surfaces models studied

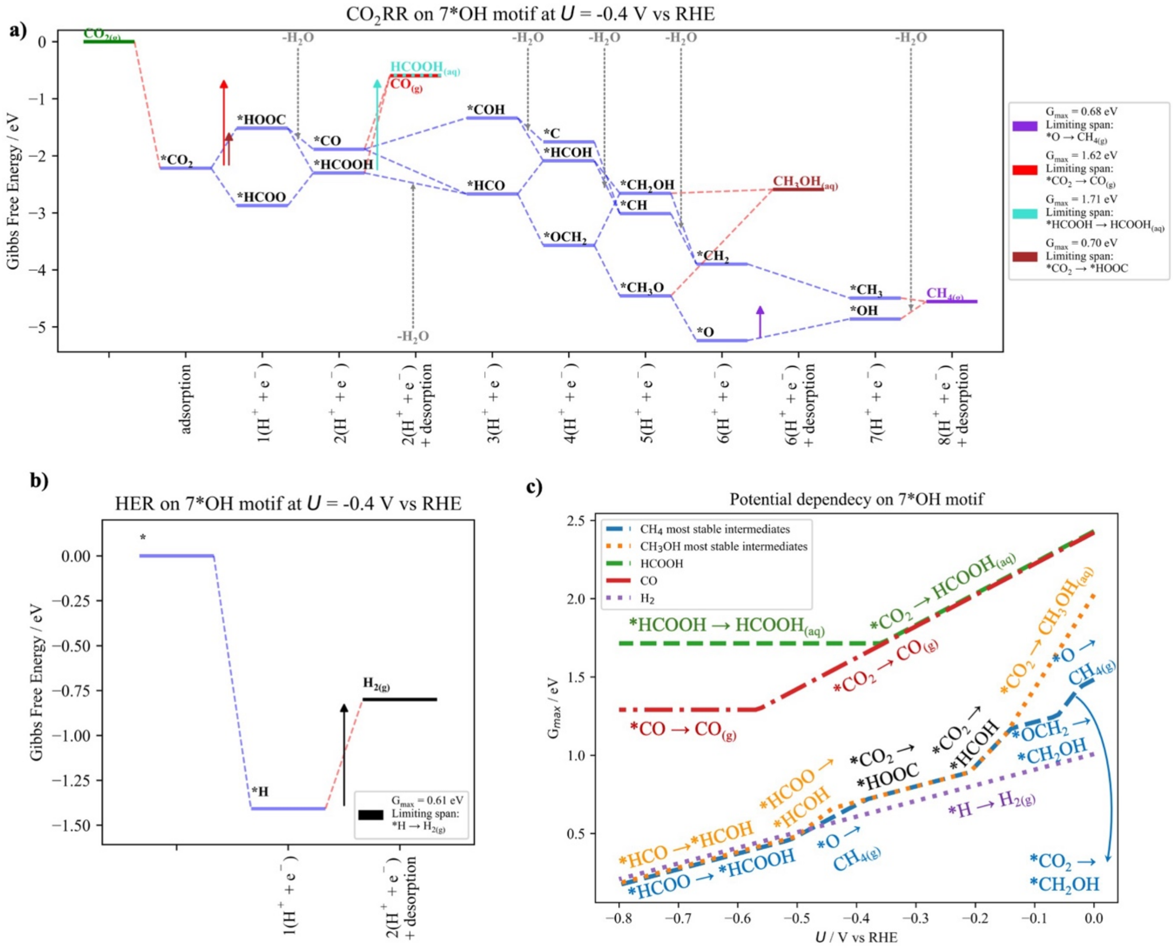

Figure S5. Gibbs free-energy diagram for the Ti_3C_2-7*OH surface model at $U = 0$ V vs RHE for **a)** CO_2RR and **b)** HER. Purple, red, cyan, brown and black arrows are used to schematically represent the limiting span for $CH_{4(g)}$, $CO_{(g)}$, $HCOOH_{(aq)}$, $CH_3OH_{(aq)}$ and $H_{2(g)}$, respectively. Details on the G_{max} and intermediates involved in the limiting span for each reaction are shown in the legend. **c)** CO_2RR and HER potential dependency of the Ti_3C_2-7*OH surface model. Green, red, orange, blue and purple lines represent the G_{max} value as a function of the applied cathodic potential (U) for the formation of $HCOOH_{(aq)}$, $CO_{(g)}$, $CH_3OH_{(aq)}$, $CH_{4(g)}$ and $H_{2(g)}$, respectively. The different labels represent the species involved in the limiting span for each reaction at each condition. Note that for two reactions comprising the same limiting span, black labels are used.

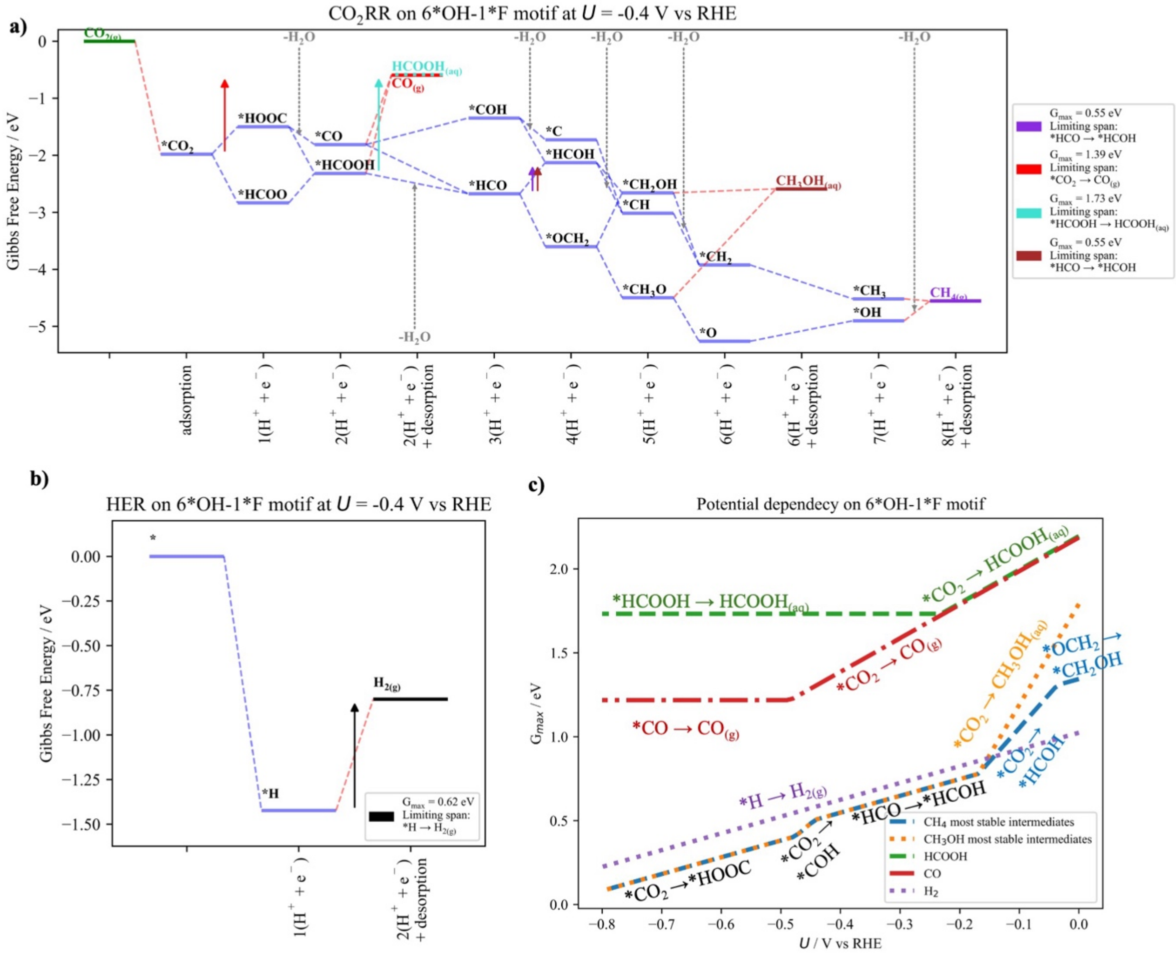

Figure S6. Gibbs free-energy diagram for the Ti_3C_2-6*OH-1*F surface model at $U = 0$ V vs RHE for **a)** CO$_2$RR and **b)** HER. Purple, red, cyan, brown and black arrows are used to schematically represent the limiting span for $CH_{4(g)}$, $CO_{(g)}$, $HCOOH_{(aq)}$, $CH_3OH_{(aq)}$ and $H_{2(g)}$, respectively. Details on the G_{max} and intermediates involved in the limiting span for each reaction are shown in the legend. **c)** CO$_2$RR and HER potential dependency of the Ti_3C_2-6*OH-1*F surface model. Green, red, orange, blue and purple lines represent the G_{max} value as a function of the applied cathodic potential (U) for the formation of $HCOOH_{(aq)}$, $CO_{(g)}$, $CH_3OH_{(aq)}$, $CH_{4(g)}$ and $H_{2(g)}$, respectively. The different labels represent the species involved in the limiting span for each reaction at each condition. Note that for two reactions comprising the same limiting span, black labels are used.

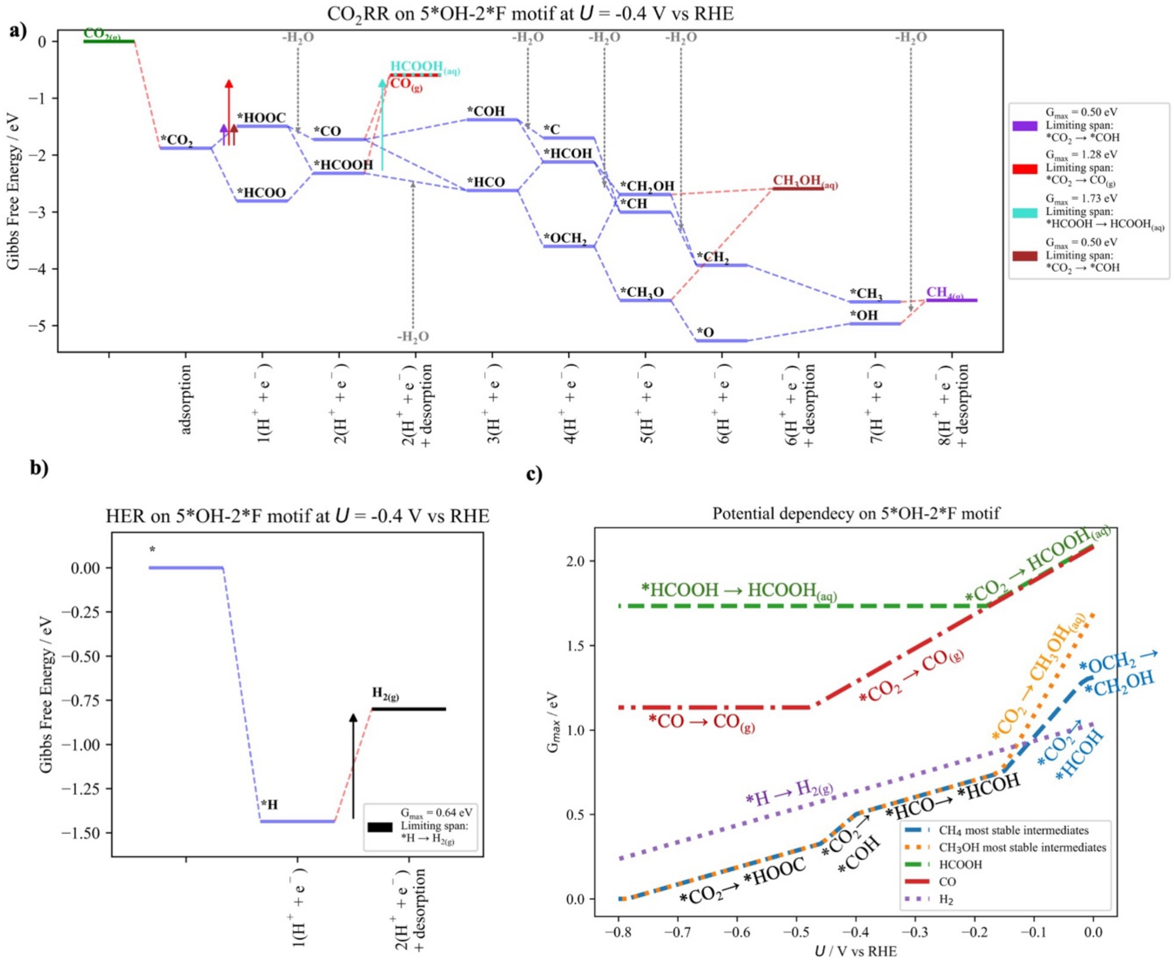

Figure S7. Gibbs free-energy diagram for the Ti_3C_2-5*OH-2*F surface model at U = 0 V vs RHE for **a)** CO$_2$RR and **b)** HER. Purple, red, cyan, brown and black arrows are used to schematically represent the limiting span for $CH_{4(g)}$, $CO_{(g)}$, $HCOOH_{(aq)}$, $CH_3OH_{(aq)}$ and $H_{2(g)}$, respectively. Details on the G_{max} and intermediates involved in the limiting span for each reaction are shown in the legend. **c)** CO$_2$RR and HER potential dependency of the Ti_3C_2-5*OH-2*F surface model. Green, red, orange, blue and purple lines represent the G_{max} value as a function of the applied cathodic potential (U) for the formation of $HCOOH_{(aq)}$, $CO_{(g)}$, $CH_3OH_{(aq)}$, $CH_{4(g)}$ and $H_{2(g)}$, respectively. The different labels represent the species involved in the limiting span for each reaction at each condition. Note that for two reactions comprising the same limiting span, black labels are used.

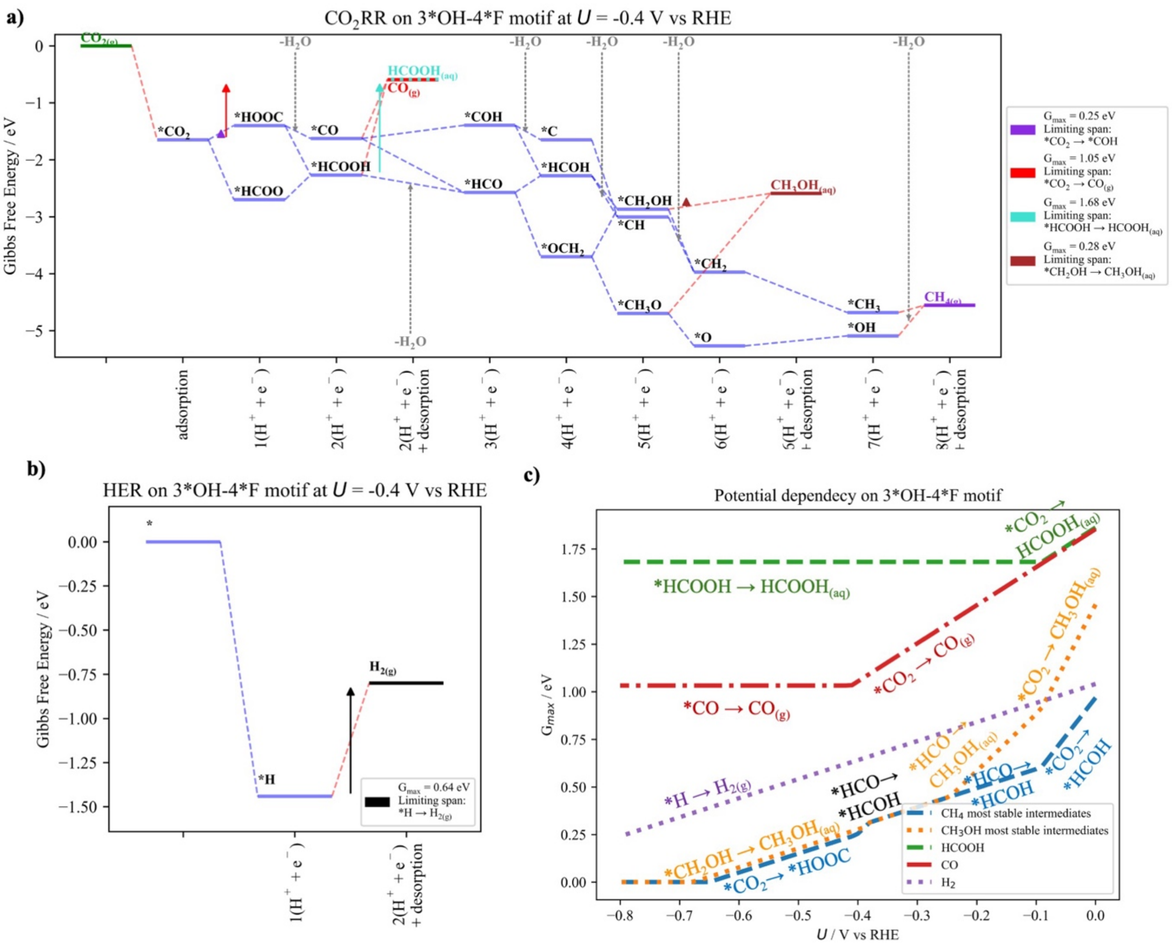

Figure S8. Gibbs free-energy diagram for the Ti_3C_2-3*OH-4*F surface model at *U* = 0 V vs RHE for **a)** CO$_2$RR and **b)** HER. Purple, red, cyan, brown and black arrows are used to schematically represent the limiting span for $CH_{4(g)}$, $CO_{(g)}$, $HCOOH_{(aq)}$, $CH_3OH_{(aq)}$ and $H_{2(g)}$, respectively. Details on the G_{max} and intermediates involved in the limiting span for each reaction are shown in the legend. **c)** CO$_2$RR and HER potential dependency of the Ti_3C_2-3*OH-4*F surface model. Green, red, orange, blue and purple lines represent the G_{max} value as a function of the applied cathodic potential (*U*) for the formation of $HCOOH_{(aq)}$, $CO_{(g)}$, $CH_3OH_{(aq)}$, $CH_{4(g)}$ and $H_{2(g)}$, respectively. The different labels represent the species involved in the limiting span for each reaction at each condition. Note that for two reactions comprising the same limiting span, black labels are used.

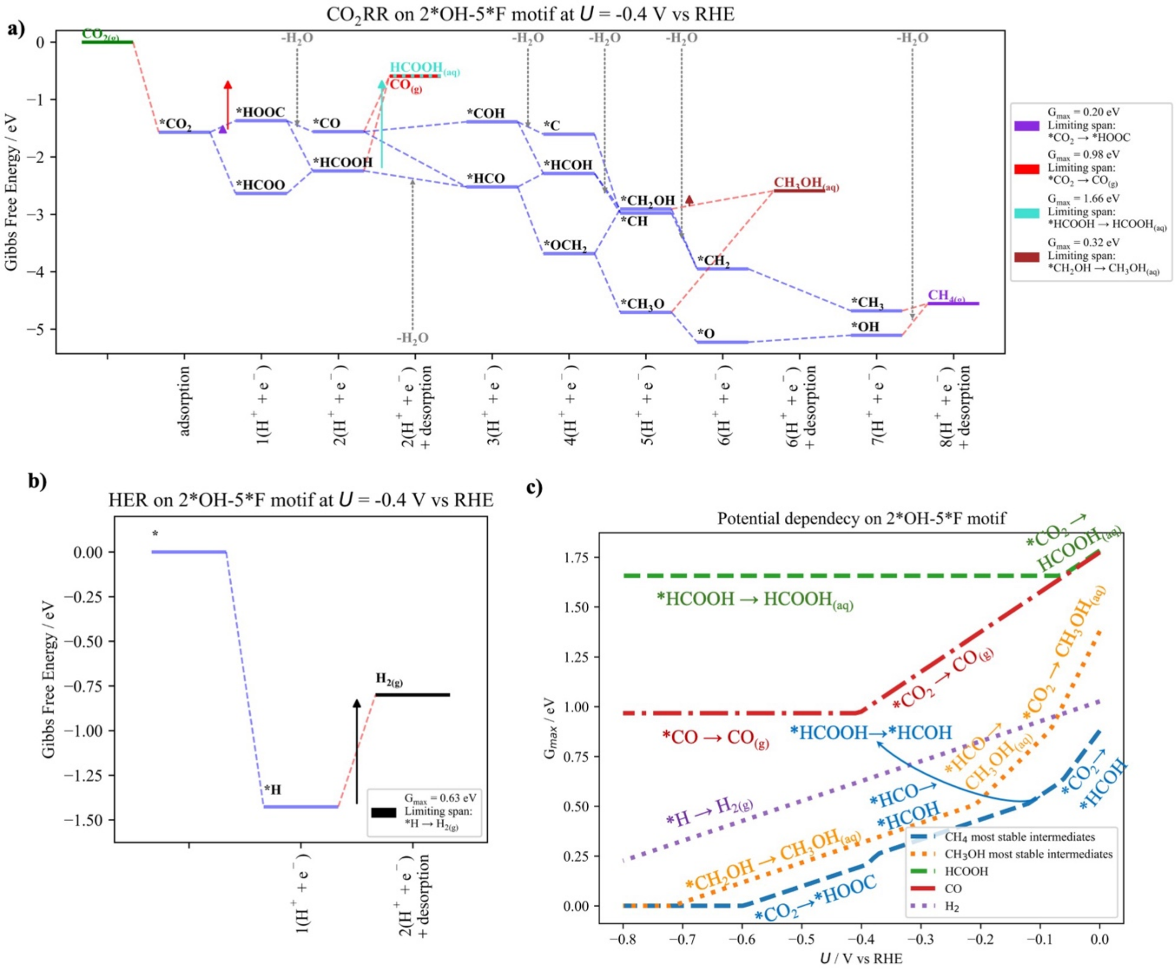

Figure S9. Gibbs free-energy diagram for the Ti_3C_2-2*OH-5*F surface model at $U = 0$ V vs RHE for **a)** CO_2RR and **b)** HER. Purple, red, cyan, brown and black arrows are used to schematically represent the limiting span for $CH_{4(g)}$, $CO_{(g)}$, $HCOOH_{(aq)}$, $CH_3OH_{(aq)}$ and $H_{2(g)}$, respectively. Details on the G_{max} and intermediates involved in the limiting span for each reaction are shown in the legend. **c)** CO_2RR and HER potential dependency of the Ti_3C_2-2*OH-5*F surface model. Green, red, orange, blue and purple lines represent the G_{max} value as a function of the applied cathodic potential (U) for the formation of $HCOOH_{(aq)}$, $CO_{(g)}$, $CH_3OH_{(aq)}$, $CH_{4(g)}$ and $H_{2(g)}$, respectively. The different labels represent the species involved in the limiting span for each reaction at each condition. Note that for two reactions comprising the same limiting span, black labels are used.

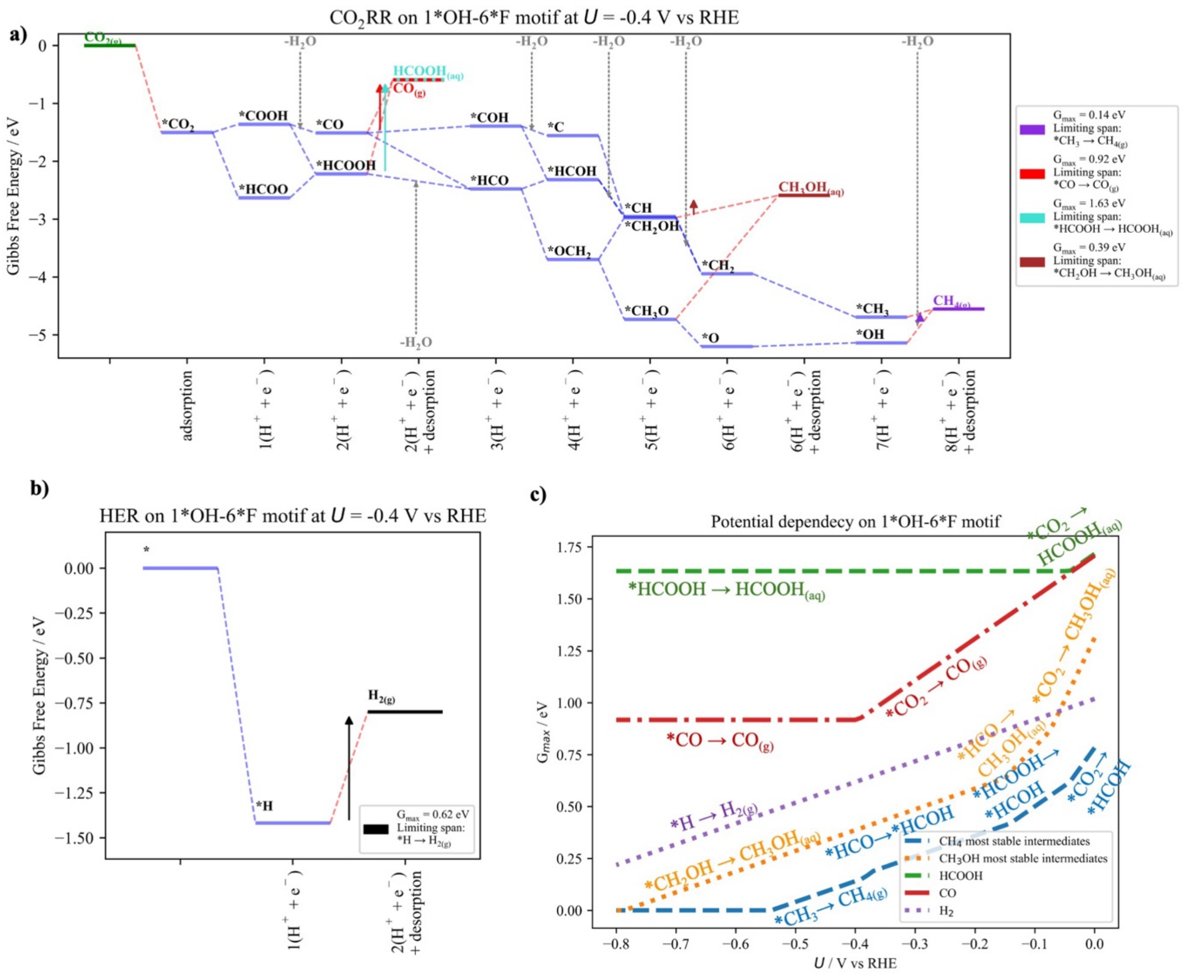

Figure S10. Gibbs free energy diagram for on the Ti_3C_2-1*OH-6*F surface model at U = 0 V vs RHE for **a)** CO_2RR and **b)** HER. Purple, red, cyan, brown and black arrows are used to schematically represent the limiting span for $CH_{4(g)}$, $CO_{(g)}$, $HCOOH_{(aq)}$, $CH_3OH_{(aq)}$ and $H_{2(g)}$, respectively. Details on the G_{max} and intermediates involved in the limiting span for each reaction are shown in the legend. **c)** CO_2RR and HER potential dependency of the Ti_3C_2-1*OH-6*F surface model. Green, red, orange, blue and purple lines represent the G_{max} value as a function of the applied cathodic potential (U) for the formation of $HCOOH_{(aq)}$, $CO_{(g)}$, $CH_3OH_{(aq)}$, $CH_{4(g)}$ and $H_{2(g)}$, respectively. The different labels represent the species involved in the limiting span for each reaction at each condition. Note that for two reactions comprising the same limiting span, black labels are used.

S8. CO_2RR free energy diagram and potential dependency for the different $Ti_3C_2T_x$ surfaces models studied considering less-stable intermediate states.

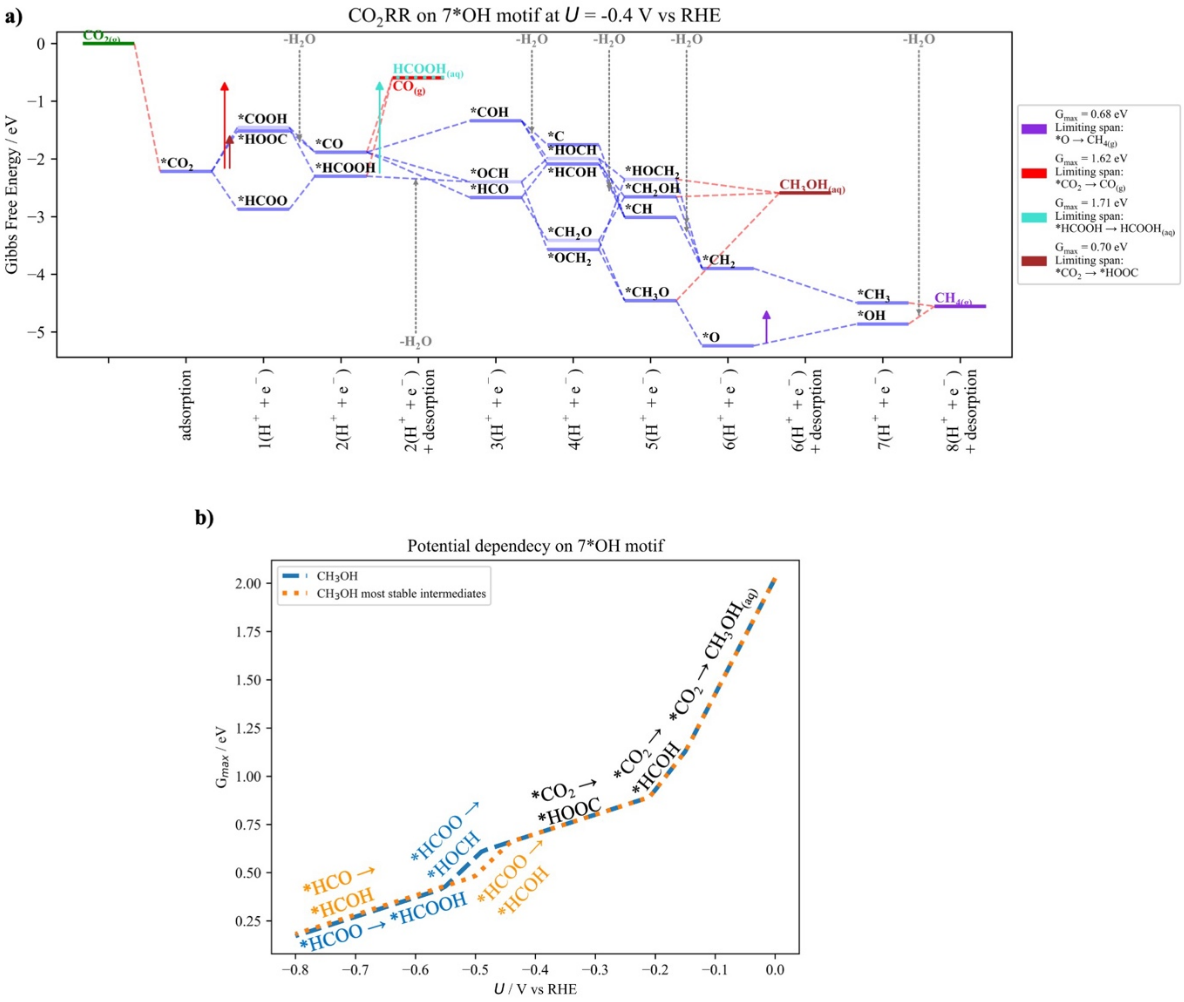

Figure S11. **a)** Gibbs free energy diagram for CO_2RR of theTi_3C_2-7*OH surface model at U = -0.4 V vs RHE considering also less stable states. Purple, red, cyan and brown arrows are used to schematically represent the limiting span for the CO_2RR to $CH_{4(g)}$, $CO_{(g)}$, $HCOOH_{(aq)}$ and $CH_3OH_{(aq)}$, respectively. For intermediates in which two states are considered, lighter bars represent the less stable state while darker bars represent the most stable state. **b)** Potential dependency of CO_2RR to CH_3OH of the Ti_3C_2-4*OH-3*F with(out) considering less-stable intermediate states in orange and blue, respectively. The different labels represent the species involved in the limiting span for each reaction at each condition. Note that for two reactions comprising the same limiting span, black labels are used.

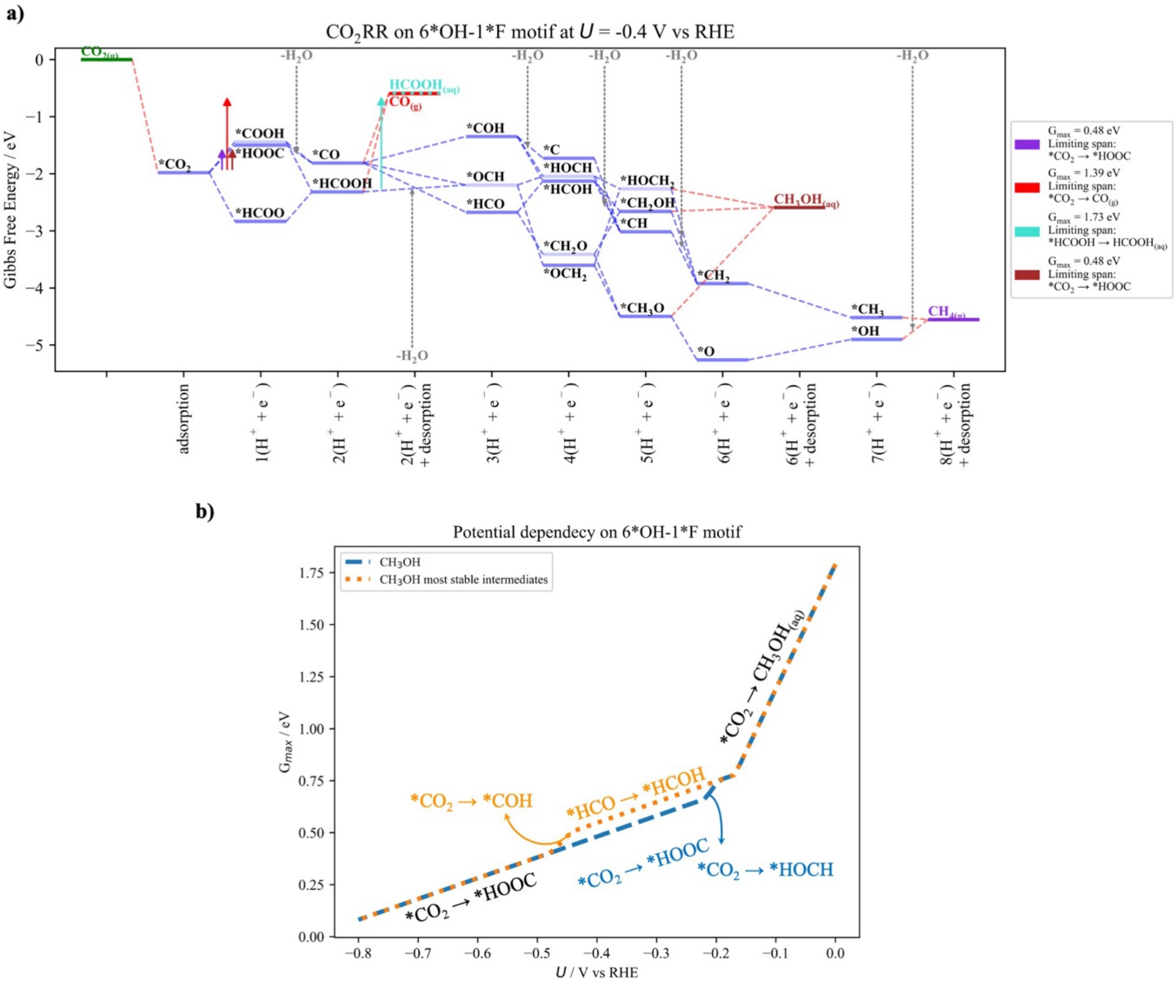

Figure S12. **a)** Gibbs free energy diagram for CO_2RR of theTi$_3$C$_2$-6*OH-1*F surface model at *U* = -0.4 V vs RHE considering also less stable states. Purple, red, cyan and brown arrows are used to schematically represent the limiting span for the CO_2RR to $CH_{4(g)}$, $CO_{(g)}$, $HCOOH_{(aq)}$ and $CH_3OH_{(aq)}$, respectively. For intermediates in which two states are considered, lighter bars represent the less stable state while darker bars represent the most stable state. **b)** Potential dependency of CO_2RR to CH_3OH of the Ti$_3$C$_2$-4*OH-3*F with(out) considering less-stable intermediate states in orange and blue, respectively. The different labels represent the species involved in the limiting span for each reaction at each condition. Note that for two reactions comprising the same limiting span, black labels are used.

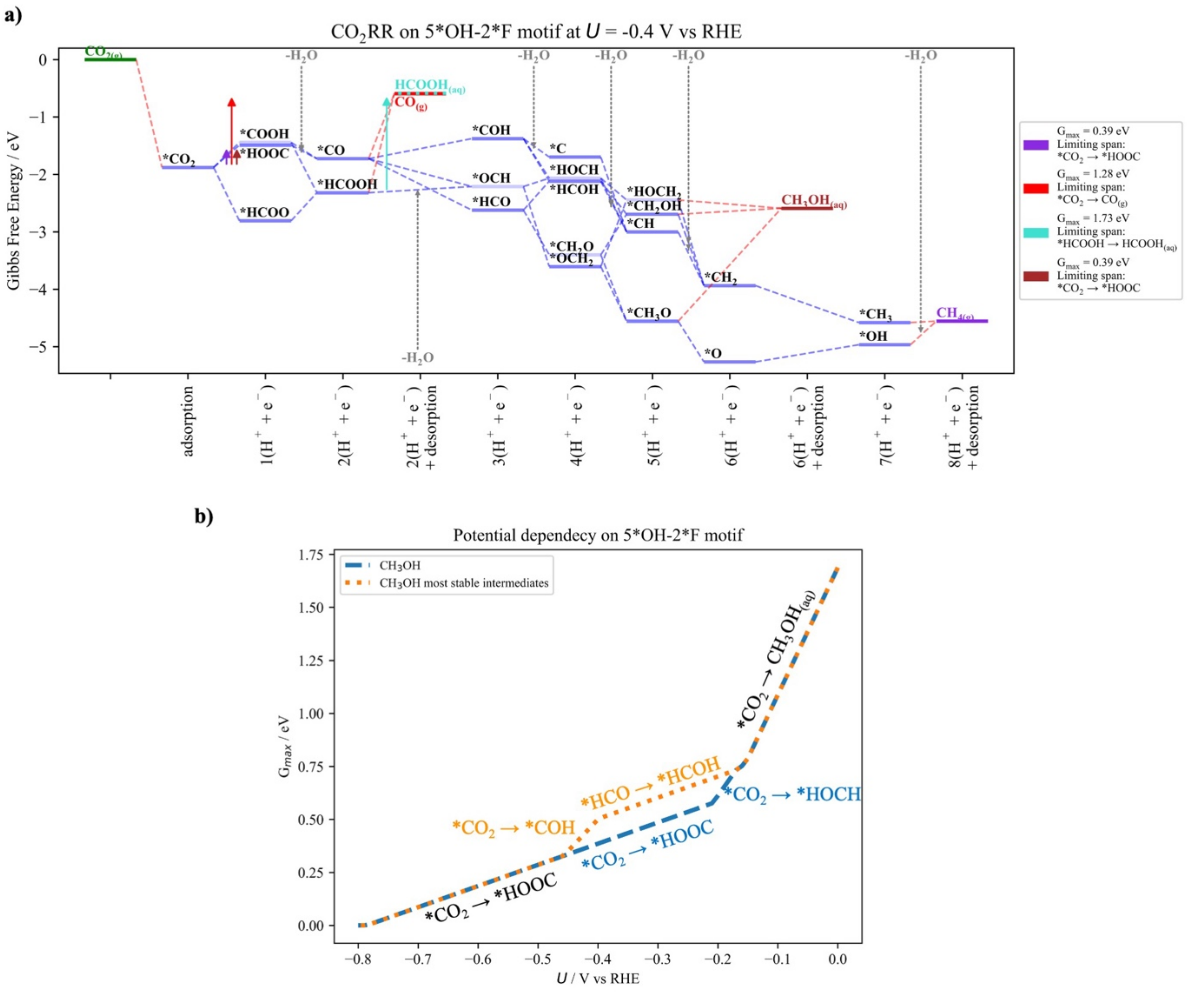

Figure S13. **a)** Gibbs free energy diagram for CO_2RR of theTi_3C_2-5*OH-2*F surface model at U = -0.4 V vs RHE considering also less stable states. Purple, red, cyan and brown arrows are used to schematically represent the limiting span for the CO_2RR to $CH_{4(g)}$, $CO_{(g)}$, $HCOOH_{(aq)}$ and $CH_3OH_{(aq)}$, respectively. For intermediates in which two states are considered, lighter bars represent the less stable state while darker bars represent the most stable state. **b)** Potential dependency of CO_2RR to CH_3OH of the Ti_3C_2-4*OH-3*F with(out) considering less-stable intermediate states in orange and blue, respectively. The different labels represent the species involved in the limiting span for each reaction at each condition. Note that for two reactions comprising the same limiting span, black labels are used.

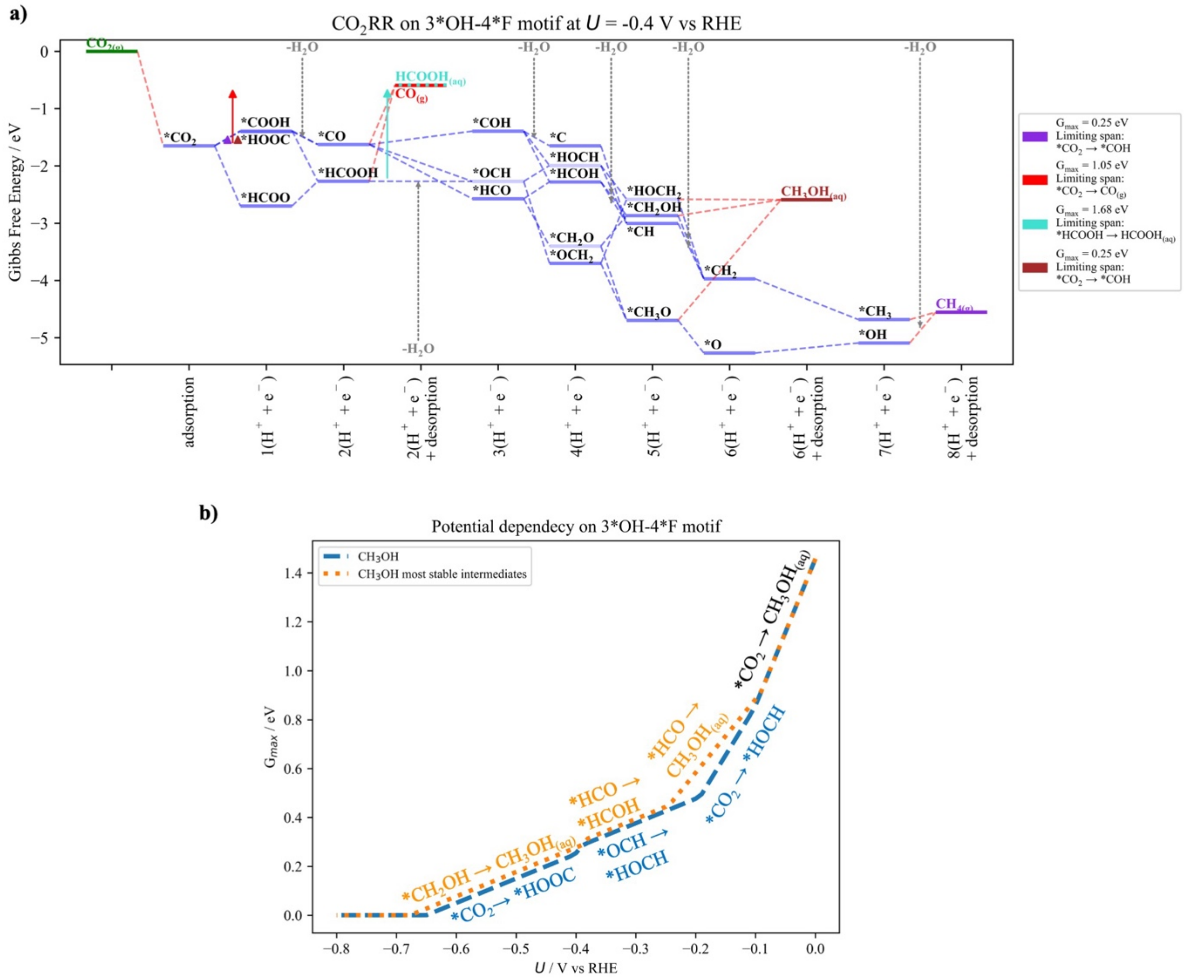

Figure S14. **a)** Gibbs free energy diagram for CO_2RR of theTi$_3$C$_2$-3*OH-4*F surface model at U = -0.4 V vs RHE considering also less stable states. Purple, red, cyan and brown arrows are used to schematically represent the limiting span for the CO_2RR to $CH_{4(g)}$, $CO_{(g)}$, $HCOOH_{(aq)}$ and $CH_3OH_{(aq)}$, respectively. For intermediates in which two states are considered, lighter bars represent the less stable state while darker bars represent the most stable state. **b)** Potential dependency of CO_2RR to CH_3OH of the Ti_3C_2-4*OH-3*F with(out) considering less-stable intermediate states in orange and blue, respectively. The different labels represent the species involved in the limiting span for each reaction at each condition. Note that for two reactions comprising the same limiting span, black labels are used.

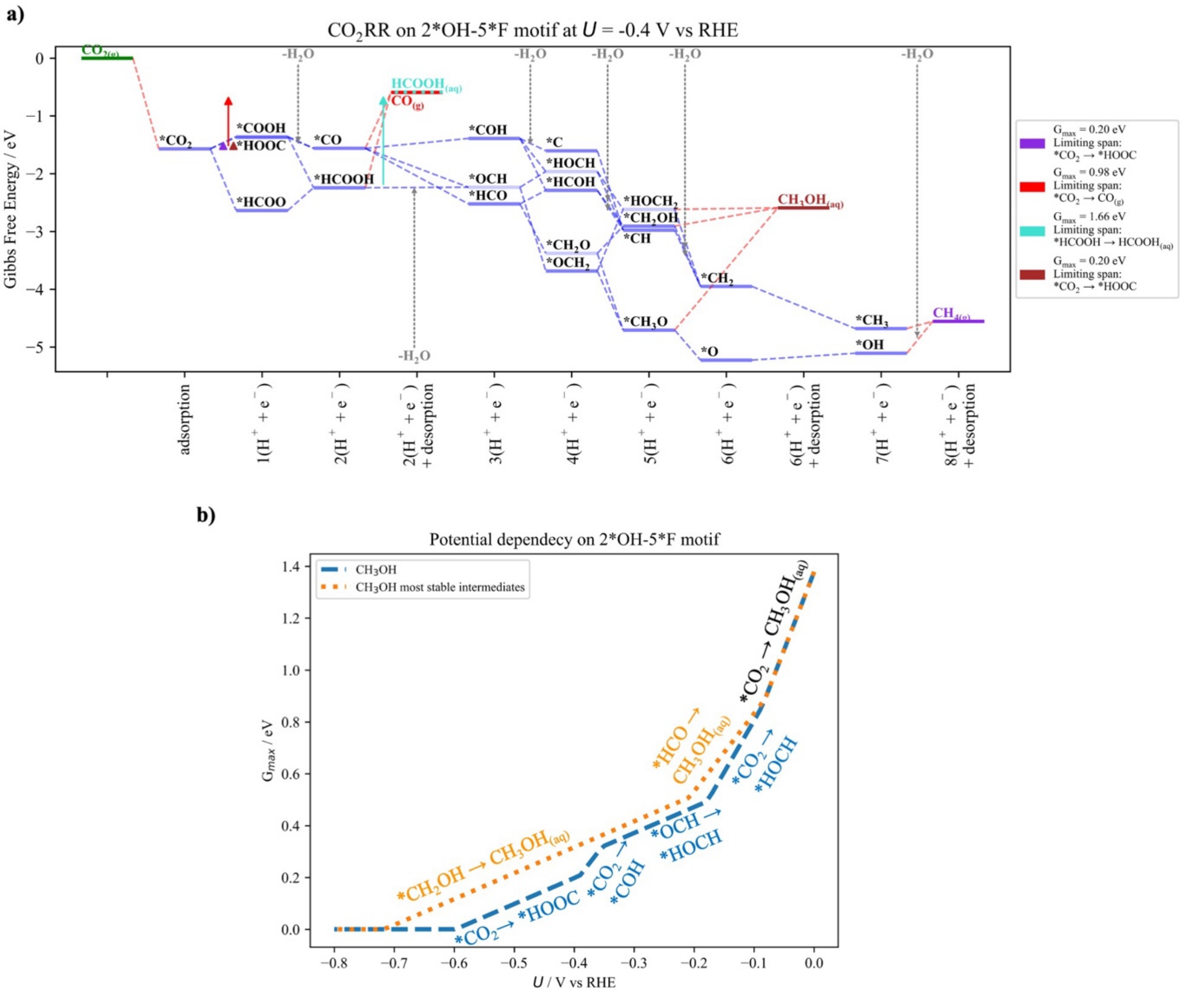

Figure S15. **a)** Gibbs free energy diagram for CO$_2$RR of theTi$_3$C$_2$-2*OH-5*F surface model at U = -0.4 V vs RHE considering also less stable states. Purple, red, cyan and brown arrows are used to schematically represent the limiting span for the CO$_2$RR to CH$_{4(g)}$, CO$_{(g)}$, HCOOH$_{(aq)}$ and CH$_3$OH$_{(aq)}$, respectively. For intermediates in which two states are considered, lighter bars represent the less stable state while darker bars represent the most stable state. **b)** Potential dependency of CO$_2$RR to CH$_3$OH of the Ti$_3$C$_2$-4*OH-3*F with(out) considering less-stable intermediate states in orange and blue, respectively. The different labels represent the species involved in the limiting span for each reaction at each condition. Note that for two reactions comprising the same limiting span, black labels are used.

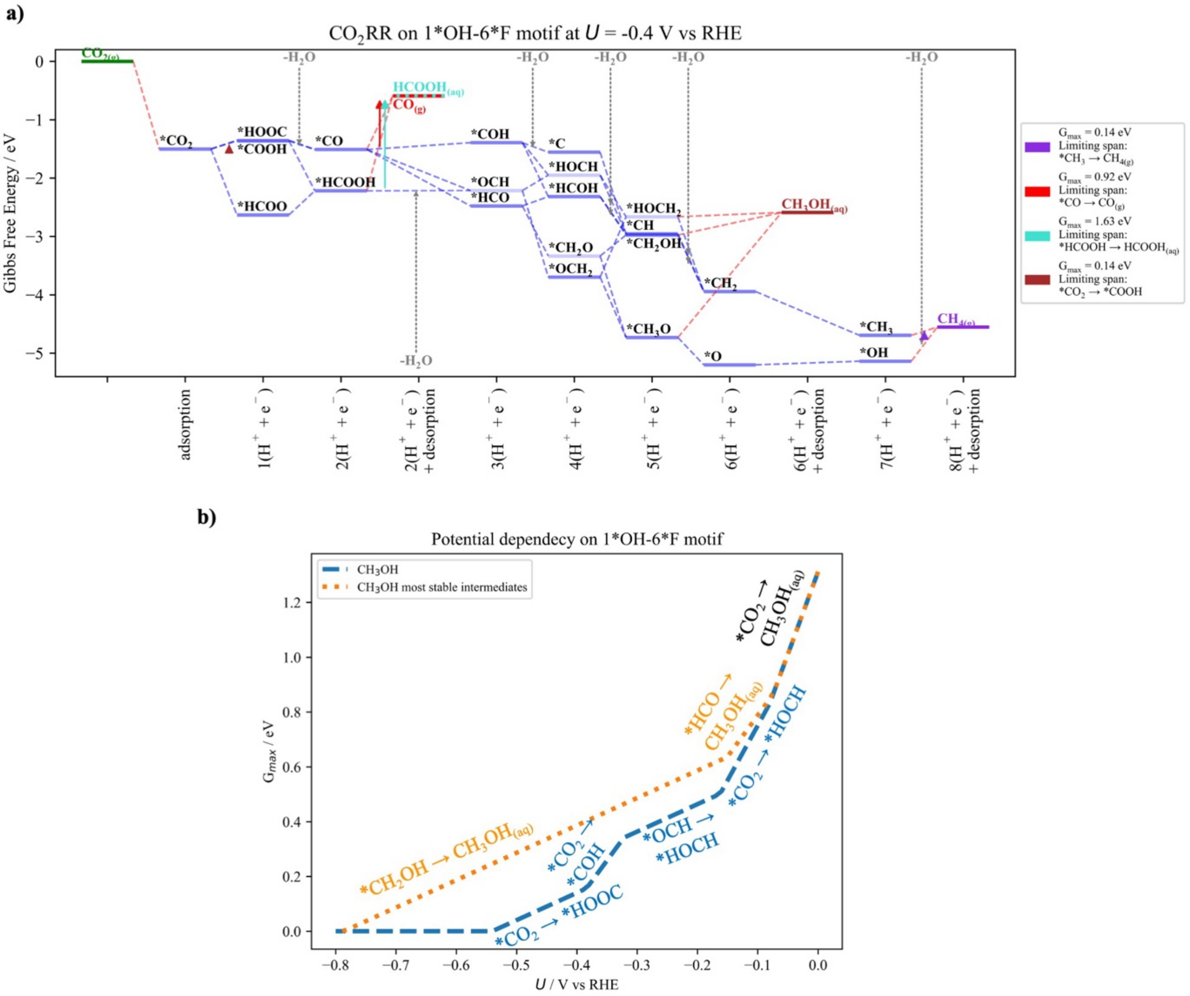

Figure S16. **a)** Gibbs free energy diagram for CO_2RR of theTi_3C_2-1*OH-6*F surface model at U = -0.4 V vs RHE considering also less stable states. Purple, red, cyan and brown arrows are used to schematically represent the limiting span for the CO_2RR to $CH_{4(g)}$, $CO_{(g)}$, $HCOOH_{(aq)}$ and $CH_3OH_{(aq)}$, respectively. For intermediates in which two states are considered, lighter bars represent the less stable state while darker bars represent the most stable state. **b)** Potential dependency of CO_2RR to CH_3OH of the Ti_3C_2-4*OH-3*F with(out) considering less-stable intermediate states in orange and blue, respectively. The different labels represent the species involved in the limiting span for each reaction at each condition. Note that for two reactions comprising the same limiting span, black labels are used.

S9. Including less-stable intermediate states can also give rise to less-active pathways.

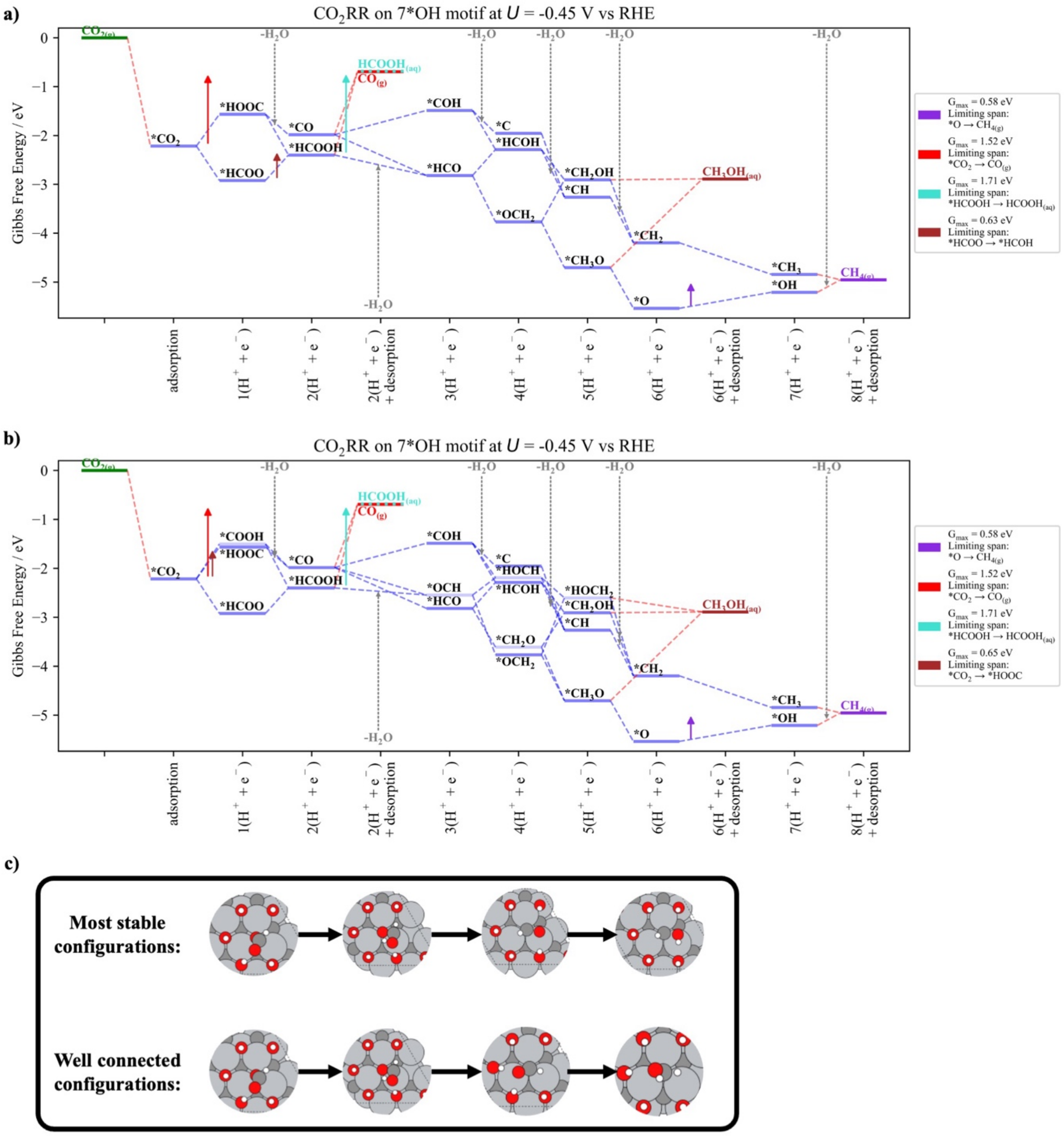

Figure S17. Gibbs free energy diagram for CO2RR of the Ti_3C_2-7*OH surface model at U = - 0.45 V vs RHE when **a)** the most stable intermediate states are considered **b)** less-stable intermediate states are also considered. Purple, red, cyan and brown arrows are used to schematically represent the limiting span for $CH_{4(g)}$, $CO_{(g)}$, $HCOOH_{(aq)}$ and $CH_3OH_{(aq)}$. Details on the G_{max} and intermediates involved in the limiting span for each reaction are shown in the legend. **c)** Graphical illustration of different reaction intermediate configurations adopted during the catalytic cycle.

Figure S17a and S17b depict the free-energy diagram for CO_2RR of the Ti_3C_2-7OH* surface model at U = -0.45 V vs RHE for the most stable intermediate states and including less-stable intermediate states, respectively. Note that, as shown in **Figure S11b**, there are no differences in the preferred pathway when including less-stable intermediate states in the analysis at $U > -0.45$ V vs RHE for the Ti_3C_2-7OH* surface model. For that reason, we have chosen $U = -0.45$ V vs RHE rather than $U = -0.40$ V vs RHE in the following analysis. **Figure S17c** shows graphically the structures of some relevent intermediates.

Let us focus on the formation of CH_3OH. A change in the G_{max} and limiting span is observed when less-stable intermediate states are considered in the analysis. As opposed to most of the situations, the fact of including less-stable intermediate states increases the G_{max}. When only the most stable intermediate states are considered, the limiting span is *HCOO → *HCOH, following the path *HCOO → *HCOOH → *HCO → *HCOH, as depicted in **Figure S17c**. However, the *HCOOH intermediate is not truly well connected to *HCO but rather to *OCH, and the pathway starting from that intermediate should be *HCOO → *HCOOH → *OCH → *HOCH as shown in **Figure S17c**. This path is now higher in energy (i.e., the free-energy span *HCOO → *HOCH is increased) and therefore the limiting span switches to $*CO_2$ → *HOOC. From these results, we conclude that for an improved mechanistic description, well-connected reaction intermediates, even if they contain less-stable intermediates, should be included in the analysis, even if they lead to less active reaction pathways.

S10. Rotational energy barriers

To gain deeper insights into the stability of less-stable intermediate states, we have calculated the Gibbs free-energy barrier of rotation between the less and most stable state for four intermediates on the seven surface models, as summarized in **Table S4**.

Table S4. Rotational energy barriers for four different intermediate species on the seven different surfaces. $\Delta G^{\neq}_{fwd}$ corresponds to the Gibbs free-energy barrier of rotation between the less and most stable states, while $\Delta G^{\neq}_{bkw}$ denotes the Gibbs free-energy barrier of the backward process.

Surface	$\Delta G^{\neq}_{fwd}$ ($\Delta G^{\neq}_{bkw}$) / eV			
	$^*OCH \rightleftharpoons {}^*HCO$	**$^*HOCH \rightleftharpoons {}^*HCOH$**	**$^*CH_2O \rightleftharpoons {}^*OCH_2$**	**$^*HOCH_2 \rightleftharpoons {}^*CH_2OH$**
7*OH	0.43 (0.70)	0.34 (0.44) [a]	0.96 (1.12)	0.16 (0.46) [a]
6*OH-1*F	0.25 (0.73)	0.42 (0.50)	0.75 (0.95)	0.11 (0.51)
5*OH-2*F	0.42 (0.83)	0.41 (0.46)	0.80 (1.00)	0.42 (0.67) [a]
4*OH-3*F	0.51 (0.82)	0.43 (0.58)	0.73 (1.04)	0.36 (0.58)
3*OH-4*F	0.51 (0.82)	0.32 (0.61)	0.74 (1.04)	0.43 (0.72)
2*OH-5*F	0.56 (0.84)	0.31 (0.64)	0.77 (1.08)	0.45 (0.74)
1*OH-6*F	0.59 (0.85)	0.31 (0.68)	0.77 (1.13)	0.43 (0.74)

[a] The force criterion used to locate the transition state has been set to 0.05 eV Å^{-1} due to convergence problems.

As observed in **Table S4**, the free-energy barriers for rotation are not excessively large. Importantly, the stability of the less-stable intermediate state are governed by the competition between the rotation to the most stable state or protonation to the most stable intermediate state, as summarized in **Table S5 – S7** for the *OCH/*HCO, *HOCH/*HCOH and $^*HOCH_2/CH_2OH$ intermediates, respectively. Note that the $^*CH_2O/^*OCH_2$ intermediates is excluded because these intermediates are not present in any of the active CO_2RR pathways. While we have not calculated the pronation energy barriers for the protonation steps, previous literature studies have reported that they are small (in the range of 0.15 eV to 0.25 eV) **[29, 30]**.

Let us start by analyzing the *OCH/*HCO intermediates (**Table S5**). Interestingly, the *HCO protonation to *HCOH is a process with a small free-energy barrier of 0.16 eV for the Cu(100) surface **[31]**. Note that, in our case, the *OCH/*HCO protonations are endergonic processes, which implies that the above value of 0.16 eV should be added to the reaction energy. From **Table S5,** it appears that, in general, the rotational energy barrier is higher than the protonation. This suggests a high stability of the less-stable intermediate state and underpins their feasibility as a new reaction channel. The only exception is found for the 7*OH and 6*OH-1*F surfaces.

We suspect that this could be the result of higher TS stabilization due to the larger number of hydrogen bonds.

Table S5. Rotational energy barriers for the *OCH/*HCO rotation on the seven different surfaces along with the reaction Gibbs free energy (ΔG_r) of the competitive protonation reactions. $\Delta G^{\neq}_{fwd}$ corresponds to the Gibbs free-energy barrier of rotation between the less and most stable intermediate states, while $\Delta G^{\neq}_{bkw}$ denotes the Gibbs free-energy barrier of the backward process.

Surface	**$\Delta G^{\neq}_{fwd}$ ($\Delta G^{\neq}_{bkw}$) / eV** ***OCH ⇌ *HCO**	**ΔG_r / eV** ***OCH + H^+ + e^- → *HOCH**	**ΔG_r / eV** ***HCO + H^+ + e^- → *HCOH**
7*OH	0.43 (0.70)	0.40	0.58
6*OH-1*F	0.25 (0.73)	0.15	0.55
5*OH-2*F	0.42 (0.83)	0.15	0.50
4*OH-3*F	0.51 (0.82)	0.20	0.36
3*OH-4*F	0.51 (0.82)	0.28	0.29
2*OH-5*F	0.56 (0.84)	0.27	0.23
1*OH-6*F	0.59 (0.85)	0.26	0.16

Let us now analyze the *HOCH/*HCOH and *HOCH$_2$/*CH$_2$OH intermediates. As shown in **Table S6** and **S7**, the protonation steps are, in general, exergonic processes, while the rotational energy barriers range from 0.31 to 0.45 eV, which are above the typical protonation values (i.e., 0.15 to 0.25 eV). Again, this suggests a high stability of the less-stable intermediate states and their feasibility as new reaction channels.

Table S6. Rotational energy barriers for the *HOCH/*HCOH rotation on the seven different surfaces along with the reaction Gibbs free energy (ΔG_r) of the competitive protonation reactions. $\Delta G^{\neq}_{fwd}$ corresponds to the Gibbs free-energy barrier of rotation between the less and most stable intermediate states, while $\Delta G^{\neq}_{bkw}$ denotes the Gibbs free-energy barrier of the backward process.

Surface	**$\Delta G^{\neq}_{fwd}$ ($\Delta G^{\neq}_{bkw}$) / eV** ***HOCH ⇌ *HCOH**	**ΔG_r / eV** ***HOCH + H^+ + e^- → *$HOCH_2$**	**ΔG_r / eV** ***HCOH + H^+ + e^- → *CH_2OH**
7*OH	0.34 (0.44) [a]	-0.36	-0.57
6*OH-1*F	0.42 (0.50)	-0.22	-0.53
5*OH-2*F	0.41 (0.46)	-0.38	-0.57
4*OH-3*F	0.43 (0.58)	-0.46	-0.53
3*OH-4*F	0.32 (0.61)	-0.59	-0.59
2*OH-5*F	0.31 (0.64)	-0.65	-0.62
1*OH-6*F	0.31 (0.68)	-0.71	-0.66

[a] The force criterion used to locate the transition state has been set to 0.05 eV Å^{-1} due to convergence problems.

Table S7. Rotational energy barriers for the *$HOCH_2$/*CH_2OH rotation on the seven different surfaces along with the reaction Gibbs free energy (ΔG_r) of the competitive protonation reactions. $\Delta G^{\neq}_{fwd}$ corresponds to the Gibbs free-energy barrier of rotation between the less and most stable intermediate states, while $\Delta G^{\neq}_{bkw}$ denotes the Gibbs free-energy barrier of the backward process.

Surface	$\boldsymbol{\Delta G^{\neq}_{fwd}}$ ($\boldsymbol{\Delta G^{\neq}_{bkw}}$) **/ eV** *$HOCH_2 \rightleftharpoons$ *CH_2OH	$\boldsymbol{\Delta G_r}$ **/ eV** *$HOCH_2 + H^+ + e^- \rightarrow CH_3OH_{(aq)}$	$\boldsymbol{\Delta G_r}$ **/ eV** *$CH_2OH + H^+ + e^- \rightarrow$ * $CH_3OH_{(aq)}$
7*OH	0.16 (0.46) [a]	-0.24	0.07
6*OH-1*F	0.11 (0.51)	-0.32	0.07
5*OH-2*F	0.42 (0.67) [a]	-0.14	0.10
4*OH-3*F	0.36 (0.58)	-0.06	0.15
3*OH-4*F	0.43 (0.72)	-0.01	0.28
2*OH-5*F	0.45 (0.74)	0.03	0.32
1*OH-6*F	0.43 (0.74)	0.07	0.39

[a] The force criterion used to locate the transition state has been set to 0.05 eV Å^{-1} due to convergence problems.

S11. CO_2RR to CO on the neighboring site of a preadsorbed CO

A graphical representation of CO and the simultaneous CO_2RR to CO happening on the neighboring site for the Ti_3C_2-7*OH is shown in **Figure S18**. Note that for the other surfaces the adsorbed intermediate structures are similar.

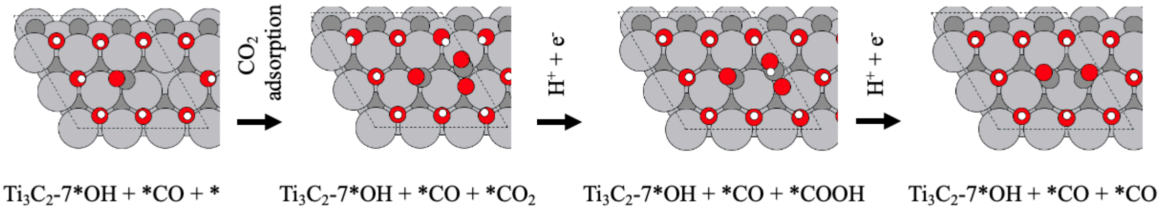

Figure S18. Graphical representation of CO and the simultaneous CO_2RR to CO happening on the neighboring site for the Ti_3C_2-7*OH surface. Light grey, dark grey, red and white spheres denote Ti, C, O and H atoms, respectively

S12. Free energy and potential dependency for CO_2RR to CO with the presence of coadsorbates

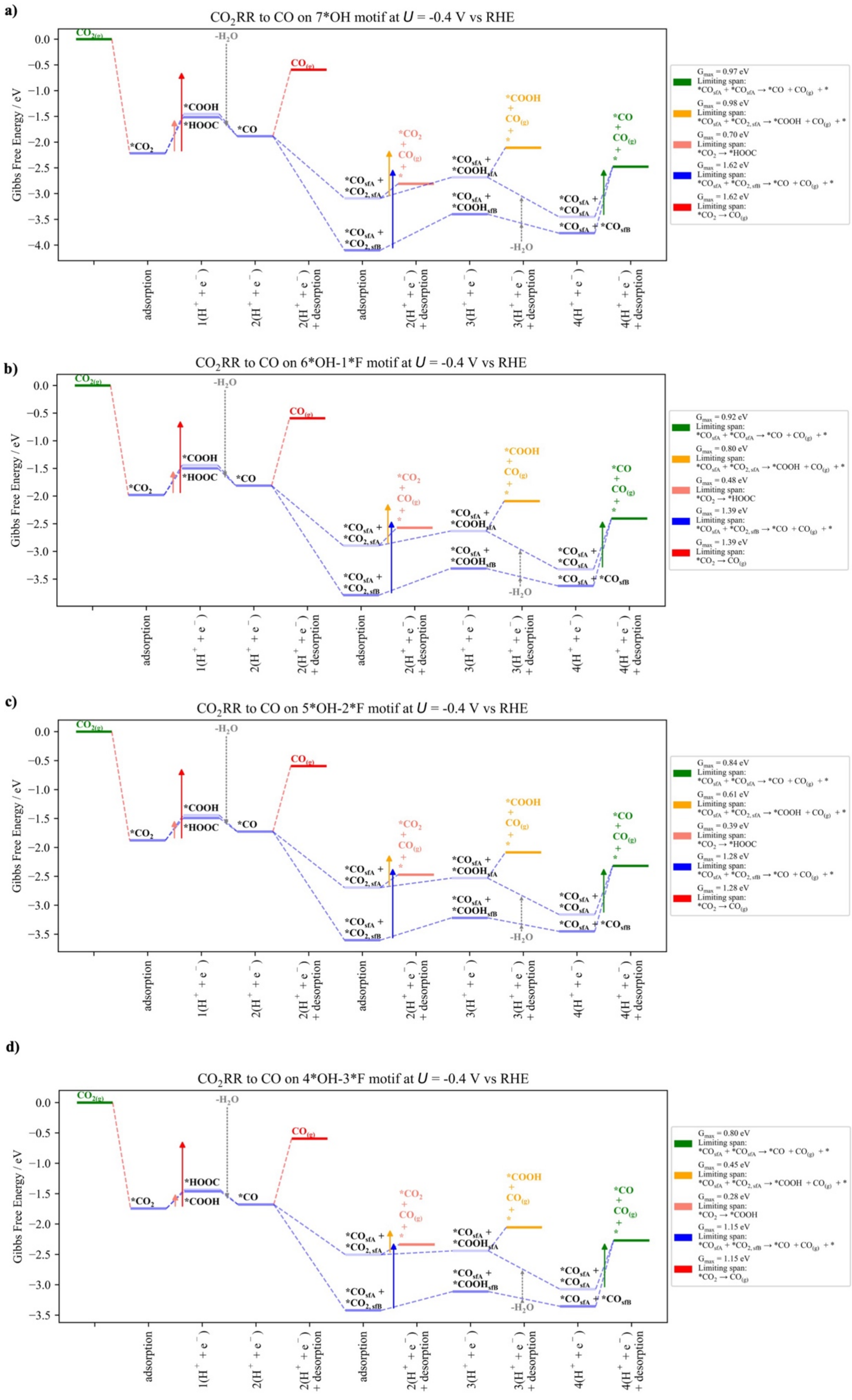

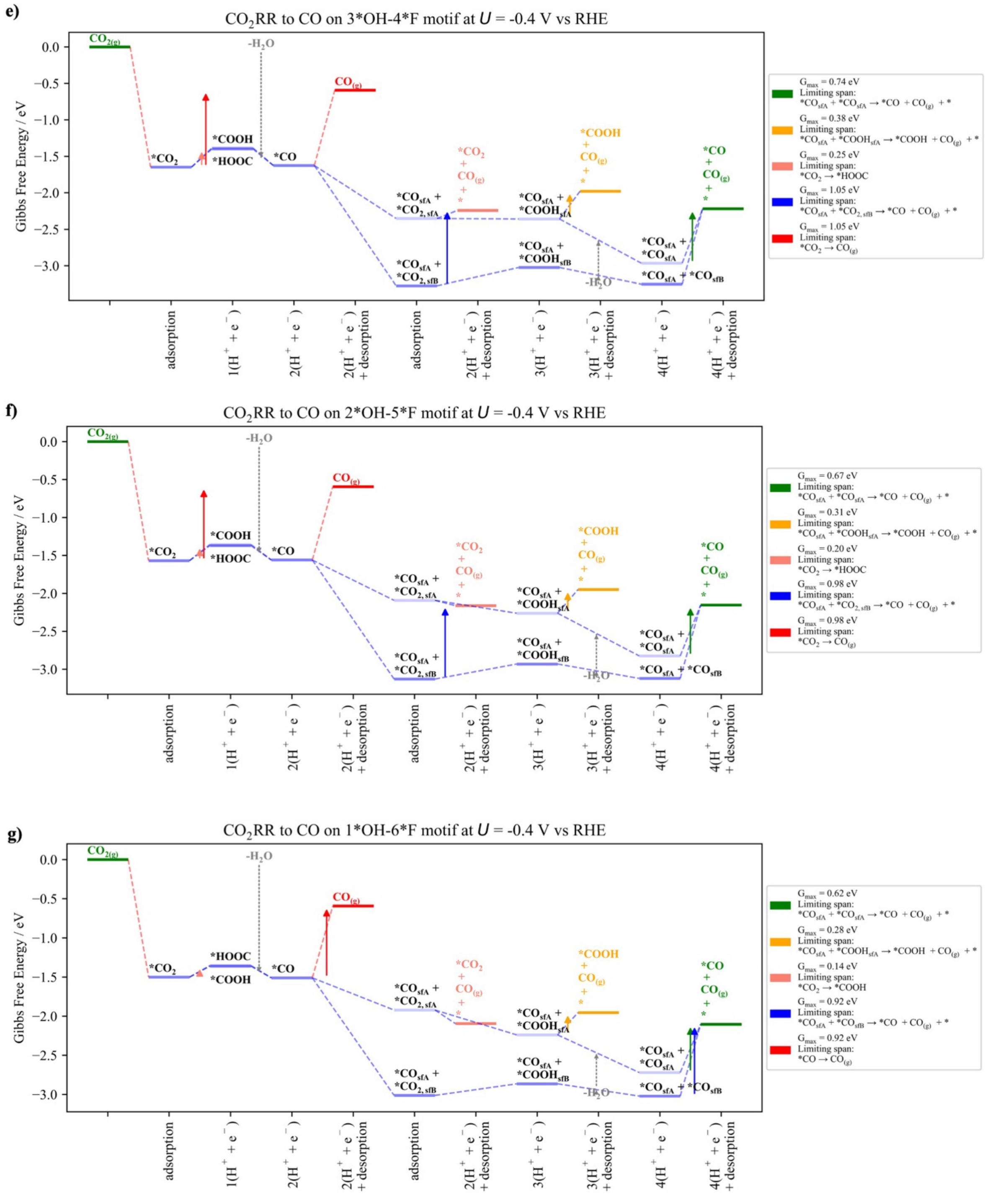

Figure S19. Gibbs free energy diagram for CO$_2$RR to CO with the presence of coadsorbate at U = -0.4 V vs RHE of **a)** Ti$_3$C$_2$-7*OH surface, **b)** Ti$_3$C$_2$-6*OH-1*F, **c)** Ti$_3$C$_2$-5*OH-2*F, **d)** Ti$_3$C$_2$-4*OH-3*F, **e)** Ti$_3$C$_2$-3*OH-4*F, **f)** Ti$_3$C$_2$-2*OH-5*F and **g)** Ti$_3$C$_2$-1*OH-6*F surface models. Green, orange, salmon and red arrows are used to schematically represent the limiting span for CO$_{(g)}$ when including *CO, *COOH, *CO$_2$ and * as coadsorbates, respectively. Blue arrow represent the limiting span for CO$_2$RR to CO when two adsorbates are not direct neighborings. Details on the G_{max} and intermediates involved in the limiting span for each reaction are shown in the legend.

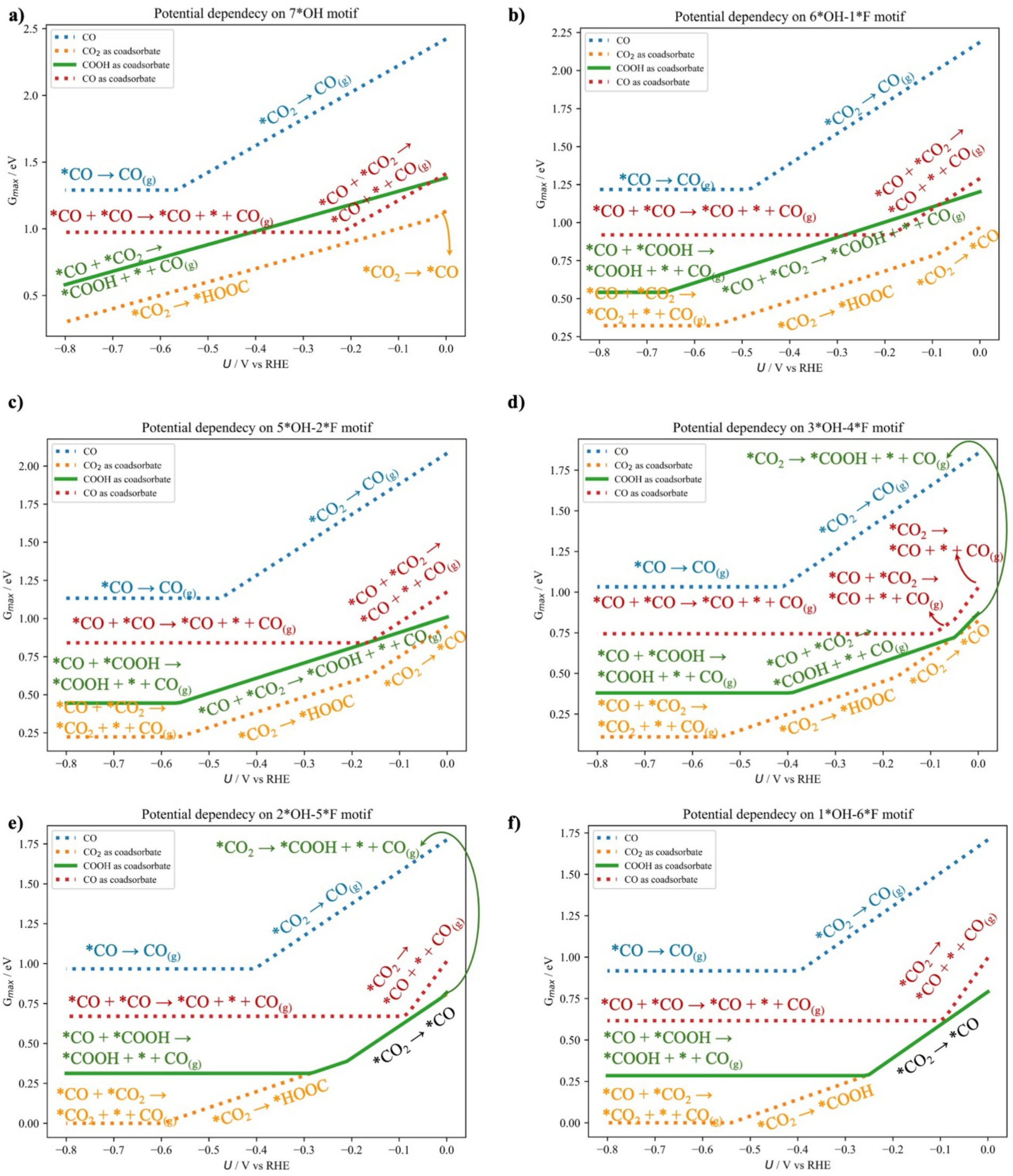

Figure S20. Potential dependency of the CO_2RR to CO with the presence of coadsorbates of **a)** Ti_3C_2-7*OH surface, **b)** Ti_3C_2-6*OH-1*F, **c)** Ti_3C_2-5*OH-2*F, **d**) Ti_3C_2-3*OH-4*F, **e)** Ti_3C_2-2*OH-5*F and **f)** Ti_3C_2-1*OH-6*F surface models.

S13. Potential dependency for HER and CO_2RR including the less-stable intermediate states and coadsorbates for the different $Ti_3C_2T_x$ surface models

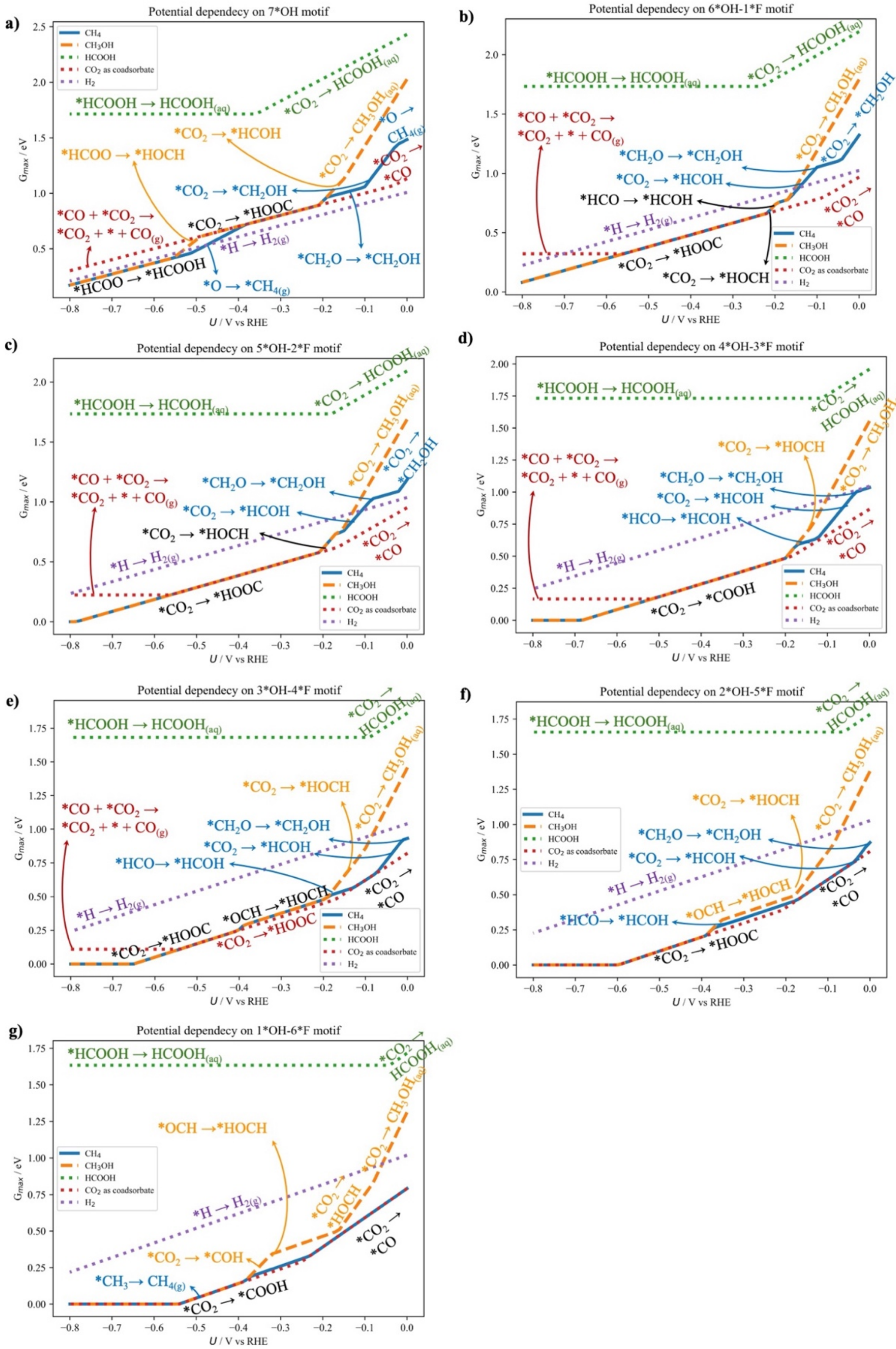

Figure S21. Potential dependency of the CO_2RR including the less stable states and the presence of coadsorbates and HER of **a)** Ti_3C_2-7*OH surface, **b)** Ti_3C_2-6*OH-1*F, **c)** Ti_3C_2-5*OH-2*F, **d)** Ti_3C_2-4*OH-3*F, **e)** Ti_3C_2-3*OH-4*F, **f)** Ti_3C_2-2*OH-5*F and **f)** Ti_3C_2-1*OH-6*F surface models.

References

---

[1] Kresse, G.; Hafner, J. Ab Initio Molecular Dynamics for Liquid Metals. Phys. Rev. B. 1993, 47, 558–561

[2] Kresse, G.; Furthmüller, J. Efficient Iterative Schemes for Ab Initio Total-energy Calculations Using a Plane-wave Basis Set. Phys. Rev. B., 1996, 54, 11169–11186

[3] Kresse, G.; Furthmüller, J. Efficiency of Ab-initio Total Energy Calculations for Metals and Semiconductors Using a Plane-wave Basis Set. Comp. Mater. Sci. 1996, 6, 15–50.

[4] Perdew, J. P.; Burke, K.; Ernzerhof, M. Generalized Gradient Approximation Made Simple. Phys. Rev. Lett., 1996, 77, 3865−3868.

[5] Grimme, S.; Antony, J.; Ehrlich, S., Krieg, H. A Consistent and Accurate Ab Initio Parametrization of Density Functional Dispersion Correction (DFT-D) for the 94 Elements H-Pu, J. Chem. Phys., 2010, 132, 154104

[6] Kresse, G.; Joubert, D. From Ultrasoft Pseudopotentials to the Projector Augmented-wave Method. Phys. Rev. B. 1999, 59, 1758–1775.

[7] Garrido Torres, J. A.; Jennings, P. C.; Hansen, M. H.; Boes, J. R.; Bligaard, T. Low-Scaling Algorithm for Nudged Elastic Band Calculations Using Surrogate Machine Learning Model. Phys. Rev. Lett., 2019, 122, 156001-5.

[8] Makov, G.; Payne, M. C. Periodic boundary conditions in ab initio calculations. Phys. Rev. B 1995, 51 (7), 4014−4022.

[9] López, M.; Exner, K. S.; Viñes, F.; Illas, F. Computational Pourbaix Diagrams for MXenes: A Key Ingredient toward Proper Theoretical Electrocatalytic Studies. Adv. Theory Simul. 2023, 6, 2200217.

[10] Mathew, K.; Sundararaman, R.; Letchworth-Weaver, K.; Arias, T. A.; Hennig, R. G. Implicit Solvation Model for Density-functional Study of Nanocrystal Surfaces and Reaction Pathways. J. Chem. Phys., 2014, 140, 084106.

[11] Mathew, K.; Kolluru, V. S. C.; Mula, S.; Steinmann, S. N.; Hennig, R. G. Implicit Self-consisten Electrolyte Model in Plane-wave Densitiy-funtional theory. J. Chem. Phys., 2019, 151, 234101.

[12] Lide, D. R. CRC Handbook of Chemistry and Physics, 85th ed.; CRC Press, 2005.

---

[13] Lozano-Reis, P.; Prats, H.; Gamallo, P.; Illas, F.; Sayós R. Multiscale Study of the Mechanism of Catalytic CO_2 Hydrogenation: Role of the Ni(111) Facets. ACS Catal. 2020, 10, 8077–8089.

[14] Nørskov, J.K.; Rossmeisl, J.; Logadottir, A.; Lindqvist, L.; Kitchin, J. R.; Bligaard, T.; Jónsson, H. Origin of the Overpotential for Oxygen Reduction at a Fuel-Cell Cathode. J. Phys. Chem. B, 2004, 108, 17886–17892.

[15] Granda-Marulanda, L.; Rendón-Calle, A.; Builes, S.; Illas, F.; Koper, M. T. M.; Calle-Vallejo, F. A Semiempirical Method to Detect and Correct DFT-Based Gas-Phase Errors and Its Application in Electrocatalysis. *ACS Catal.* 2020, 10, 12, 6900–6907

[16] Urrego-Ortiz, R.; Builes, S.; Illas, F.; Calle-Vallejo, F. Gas-phase Errors in Computational Electrocatalysis: a Review. *EES Catal.*, 2024, **2**, 157–179.

[17] Tayyebi, E.; Exner, K. S. Refining Free-Energy Calculations for Electrochemical Reactions: Unveiling Corrections beyond Gas-Phase Errors for Solvated Species and Ions. *J. Phys. Chem. C* **2024**, 128, 33, 13732–13742.

[18] Krishnan, S.; Marimuthu, S.; Singh, M. K.; Rai, D. K. Two-dimensional $Ti_3C_2T_X$ MXene Nanosheets for CO_2 Electroreduction in Aqueous Electrolytes. Enegy, Adv. 2023, 2, 1166

[19] Ooka, H.; Huang, J.; Exner, K. S. The Sabatier Principle in Electrocatalysis: Basics, Limitations, and Extensions. Front. Energy Res., 2021, 9, 654460.

[20] Wang, S.; Petzold, V.; Tripkovic, V.; Kleis, J.; Howalt, J. G.; Skúlason, E.; Fernández, E. M.; Jones, G.; Toftelund, A.; Falsig, H.; Björketun, M.; Studt, F.; Abild-Pedersen, F.; Rossmeisl, J.; Norskov, J. K.; Bligaard, T.; Universal Transition State Scaling Relations for (De)Hydrogenation over Transition Metals. Phys. Chem. Chem. Phys., 2011,13, 20760-20765

[21] Wang, S.; Temel, B.; Shen, J.; Jones, G.; Grabow, L. C.; Studt, F.; Bligaard, T.; Abild-Pedersen, F.; Christensen, C. H.; Norskov, J. K. Universal Bronsted-Evans-Polanyi Relations for C-C, C-O, C-N, N-O, N-N and O-O Dissociation Reactions. Catal. Lett. 2011, 141, 370-373.

[22] Johnson, L.R.; Sridhar, S.; Zhang, L.; Fredrickson, K. D.; Raman, A. S.; Jang, J.; Leach, C.; Padmanabhan, A.; Price, C. C.; Frey, N. C.; Raizada, A.; Rajaraman, V.; Saiprasad, S. A.; Tang, X.; Vojvodic, A. Mxene Materials for the Electrochemical Nitrogen Reduction-Functionalized or Not? ACS Catal., 2020, 10, 253–264.

[23] Deng, W.; Zhang, P.; Qiao, Y.; Kastlunger, G.; Govindarajan, N.; Xu, A.; Chorkendorff, I.; Seger, B.; Gong, J. Unraveling the rate-determining step of C2+ products during electrochemical CO reduction. Nat. Commun., 2024, 15, 892.

[24] Li, X.; Cheng, Z.; Wang, X. Unverstanding the Mechanism of the Oxygen Evolution Reaction with Consideration of Spain. Electrochem. Energy Rev., 2021, 4, 136–145.

[25] Exner, K. S. Standard-state Entropies and their Impact on the Potential-dependent Apparent Activation Energy in Electrocatalysis J. Energy Chem., 2023, 83, 247–254.

[26] Kozuch, S.; Shaik, S.; How to Conceptualize Catalytic Cycles? The Energetic Span Model. Acc. Chem. Res., 2011, 44, 101–110.

[27] Exner, K. S. A universal Descriptor for the Screening of Electrode Materials for Multiple-Electron Processes: Beyond the Thermodynamic Overpotential. ACS Catal., 2020, 10, 12607–12617.

[28] Razzaq, S.; Exner, K. S. Materials Screening by the Descriptor $G_{max}(\eta)$: The Free-Energy Span Model in Electrocatalysis. ACS Catal., 2023, 13, 1740–1758

[29] Janik, M. J.; Taylor, C. D.; Neurock, M. First-Principles Analysis of the Initial Electroreduction Steps of Oxygen over Pt(111). *J. Electrochem. Soc.,* **2009**, 156, B126-B135.

[30] Tripkovic, V.; Skúlason, E.; Siahrostmai, S.; Nørskov, J. K.; Rossmeisl, J. The Oxygen Reduction Reaction Mechanism on Pt(111) from Density Functional Theory Calculations. *Electrochim. Acta*, **2010**, 55, 7975-7981.

[31] Cheng, T.; Xiao, H.; Goddard, W. A. Free-Energy Barriers and Reaction Mechanisms for the Electrochemical Reduction of CO on the Cu(100) Surface, Including Multiple Layers of Explicit Solvent at pH 0. *J. Phys. Chem. Lett*., **2015**, 23, 4767-4773.